Politecnico di Milano

SCHOOL OF INDUSTRIAL AND INFORMATION ENGINEERING
Master of Science – Energy Engineering

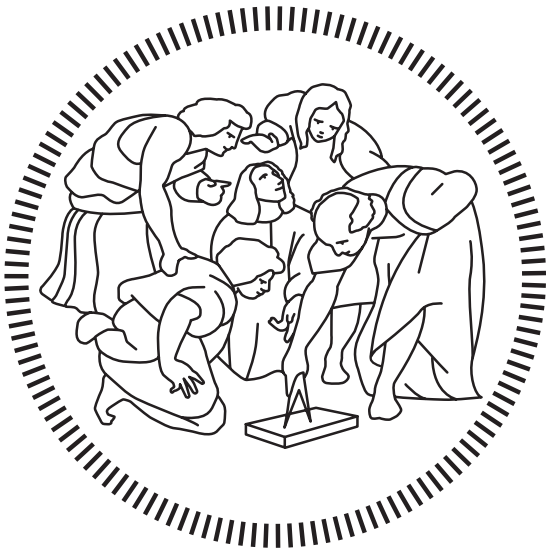

CFD Modelling of the Borexino Solar Neutrino Detector: Investigation of the Inner Vessel Fluid-dynamics and Polonium Concentration

Supervisor
Prof. RICCARDO MEREU

Co-Supervisor
Ing. VALENTINO DI MARCELLO

Candidate
ROMOLO BENATI – 892769

Academic Year 2018 – 2019

Acknowledgements

I would like to thank, fist of all, professor Mereu, who taught me what does it mean to work in a professional environment. Second, thank you Valentino for the constant and clear support.
Thanks to my parents and my family, you pushed me in every moment towards the growth.
Thank you very much to all the colleagues who shared with me this travel through the Politecnico di Milano. Thank you Matilde and *VW12*. A hug to Davide, Fabi, Baba, Marti, Gico, Paolo, Nico and the other 200 people. Good luck.
Thank you Camilla and all the great people met in Norway. A special thanks to mon frère francais and mi hermana mexicana, Alexis and Alajandra.
Thank you Mattia for the help with LaTeX... and for the rest. Thank you Agnese for the English. Thank you Sbocc and the artists. Thanks to Villa Oliva, that hosted me for the writing.
Of course, thanks to the GNAM Society.

Sommario

Borexino è un rilevatore di neutrini ad alta precisione situato nei Laboratori Nazionali del Gran Sasso, in Abruzzo. Livelli straordinari di radiopurezza sono stati raggiunti ed hanno permesso la misurazione di neutrini prodotti da diverse reazioni di fusione nucleare nel Sole. In ogni caso, la presenza di contaminanti nel suo Inner Vessel (IV), come bismuto e polonio, genera eventi di fondo che impediscono il rilevamento dei neutrini originati nel ciclo CNO. Il moto di questi contaminanti è strettamente collegato alla fluidodinamica; è stato ricercato un metodo che permetta quindi di mettere in relazione le condizioni termiche esterne a Borexino ed i movimenti del fluido contenuto. Le asimmetrie della temperatura dell'aria che circonda il rilevatore sono la causa della convezione naturale interna. Un modello CFD bidimensionale ed uno tridimensionale sono stati ideati affiché possano riprodurre la fluidodinamica dell'IV. Le sonde di temperatura, posizionate sia esternamente sia internamente a Borexino, hanno fornito i dati di input per il software; la posizione esatta di un sensore rimane però sconosciuta e crea lieve incertezza nelle condizioni al contorno. I dati considerati sono relativi ad un periodo tra Gennaio e Febbraio 2017. Conseguentemente, il modello matematico e quello numerico sono descritti. Diverse analisi di sensitività, sulla configurazione della mesh e sul time-step, sono state portate a termine con lo scopo di incrementare la precisione dei risultati e di capirne la validità. Il modello 2D mostra la presenza di flussi orizzontali stratificati. Il 3D conferma il trend e rivela che il fluido sta effettivamnete ruotando attorno all'asse verticale. Le componenti verticali della velocità sono in entrambi i casi molto deboli e probabilmente legate al rumore numerico; nel sistema tridimensionale inoltre, dei movimenti ascensionali al bordo sono rilevati, in accordo con passate osservazioni sulla migrazione del polonio. Sempre nel caso 3D, la maggiore dimensione media della cella porta a velocità di un ordine di grandezza più elevato rispetto al 2D. Questo fatto ovviamente influenza la distribuzione finale di polonio. In quel periodo, la concentrazione reale di ^{210}Po vede un minimo nella parte alta del volume preso in esame. Mentre il modello di trasposto bidimensionale ha ottenuto una buona corrispondenza con i dati misurati, sia qualitativa sia quantitativa, quello tridimensionale presenta una concentrazione di gran lunga superiore. E' possibile però affermare che i risultati 3D stiano gradualmente avvicinandosi a quelli 2D, un ruolo fondamentale è giocato dalla griglia computazionale.

Parole chiave:
Computational Fluid Dynamics
Rilevatore di neutrini
Convezione naturale
Borexino

Abstract

Borexino is a high-precision neutrinos detector located in the Laboratori Nazionali del Gran Sasso, in Abruzzo. Extraordinary radio-purity levels have been reached and permitted to measure neutrinos fluxes produced by several fusion reactions occurring in the Sun. Anyway, the presence of contaminants in its Inner Vessel (IV), such as bismuth and polonium, generates background events which can worsen the detection of the neutrinos related to the CNO-cycle. The motion of these contaminants is strictly linked to the fluid-dynamics; a method to correlate the external thermal environment and the internal fluid movements is being searched. The temperature asymmetries of the air surrounding the detector are the drivers of the inner natural convection. A bi-dimensional and a tri-dimensional Computational Fluid Dynamics (CFD) models were designed in order to reproduce the fluid-dynamics of the IV. The temperature probes, arranged outside and inside Borexino, provided the input data for the software; different data interpolations were used because of the uncertain position of one particular probe. Data from a period among January and February 2017 have been considered. Thus, the mathematical and the numerical models are carefully described. Several sensitivity analysis, on the mesh configuration and on the time-step, have been then computed with the purpose of understanding the validity and increasing the precision of the results. The 2D model shows the presence of horizontal stratified flows. The 3D model confirms the trend and reveals that the fluid is spinning around the central vertical axis. The vertical velocity components in the bulk are in both cases very weak and probably related to numerical noise; in the tri-dimensional system anyway, some vertical movements at the border are present and are in agreement with previous observations of the polonium migration. In the 3D case also, the larger average cell size generates a velocity intensity of a higher order of magnitude compared to the 2D. This certainly affects the final polonium distribution. In that period, the ^{210}Po real concentration shows a minimum in the topmost part of the volume. While the bi-dimensional transfer model obtains qualitatively and quantitatively a good match with the measured data, the tri-dimensional one presents an extremely higher concentration. It is possible to say that the 3D results are slowly approaching the 2D ones; key role is played by the computational grid.

Keywords:
Computational Fluid Dynamics
Neutrino detector
Natural convection
Borexino

Contents

Acknowledgements **iii**

Sommario **v**

Abstract **vii**

Contents **x**

List of Figures **xii**

List of Tables **xiii**

Introduction **1**

1 Borexino detector and background stability problem **3**
1.1 Borexino detector 3
1.2 Background stability 6
1.3 Borexino Thermal Monitoring & Management System (BTMMS) . . 8

2 Borexino thermal environment and previous simulations **11**
2.1 Borexino thermal evolution 11
2.2 Previous CFD models and simulations 12

3 Governing equations for the mathematical models **17**
3.1 Pseudocumene fluid-dynamic model 17
3.2 ^{210}Po mass transfer model 18

4 2D and 3D numerical domains and models setup **19**
4.1 Mesh generation and geometrical model description 19
4.2 Initial and boundary conditions 22
4.3 Numerical model setup 24
4.4 ^{210}Po mass transfer model 26

5 Results of the 2D cases **27**
5.1 *Water Ring* simulations 27
5.2 Cell size sensitivity analysis 30
5.3 Overall comparison of the 2D Polonium concentration 35

6 Results of the 3D cases **37**
6.1 Cell size sensitivity analysis 38

6.2 Time-step sensitivity analysis 48
6.3 Boundary layer sensitivity analysis on the very fine mesh 49
6.4 Final simulation: extra fine mesh 52
6.5 3D Polonium concentration 58

Conclusion and perspectives **61**

Acronyms **63**

Bibliography **67**

List of Figures

Figure 1.1 Schematic drawing of the Borexino detector 4
Figure 1.2 PC and PPO molecules 5
Figure 1.3 DMP molecule 6
Figure 1.4 LTPS probes positions. Division by phase of installation. . . . 9
Figure 1.5 Sample of the TIS material 10

Figure 2.1 Initial temperature distribution for the IV. Picture taken from the 3D convective simulation of the IV (see below) of February 2017. 12
Figure 2.2 Water Ring model structure. 14

Figure 4.1 Boundary layer comparison for the 2D cases. 20
Figure 4.2 Boundary layer meshes comparison. 21
Figure 4.3 Simplified flow chart of the BCs imposition. 22
Figure 4.4 Mapping function schematic behaviour. 23
Figure 4.5 Area division for the linear interpolation in logical coordinates. 24

Figure 5.1 *Water Ring* simulation accuracy check – South side. 28
Figure 5.2 *Water Ring* simulation accuracy check – North side. 29
Figure 5.3 30
Figure 5.4 Velocity magnitude. From the left: base case, 1° and 2° interpolation. 31
Figure 5.5 Horizontal velocities. From the left: base case, 1° and 2° interpolation. 31
Figure 5.6 Vertical velocities. From the left: base case, 1° and 2° interpolation. 32
Figure 5.7 Schematic behaviour of the boundary fluid dynamics. 32
Figure 5.8 Initial velocity magnitude evolution – Base case. 33
Figure 5.9 Velocity magnitude. From the left: base case and 2° interpolation. 34
Figure 5.10 Horizontal velocity. From the left: base case and 2° interpolation. 34
Figure 5.11 Vertical velocity. From the left: base case and 2° interpolation. 35
Figure 5.12 Vertical velocity distribution. 35
Figure 5.13 Polonium distribution over the vertical coordinate of the Fiducial Volume. 36

Figure 6.1 Complete scheme of the 3D analysis. 38
Figure 6.2 39
Figure 6.3 Velocity magnitude – ZX plane. From the left: 2.4M, 5M and 10M. 39
Figure 6.4 Y velocity – ZX plane. From the left: 2.4M, 5M and 10M. . . 40

Figure 6.5 Velocity vectors coloured by V magnitude – XY plane, Z=5.85m. From the left: 2.4M and 10M. 40
Figure 6.6 Z velocity – ZX plane. From the left: 2.4M, 5M and 10M. . . 41
Figure 6.7 Velocity magnitude and temperature evolution at Z=5.85m. . 41
Figure 6.8 Schematic behaviour of the boundary fluid dynamics – ZX and ZY planes. 42
Figure 6.9 2.4M of cells – 129'000s 44
Figure 6.10 10M of cells – 129'000s 44
Figure 6.11 Position of the BCs check points for the comparison. 46
Figure 6.12 BCs at the points N°3, N°5 and N°7. 46
Figure 6.13 Interpolation velocity magnitude evolution. From the top: 2.4M, 5M and 10M. 47
Figure 6.14 Punctual velocity trend – $X = 4.65m$ / $Z = 5.85m$ 47
Figure 6.15 Velocity magnitude evolution with different time-steps at Z=5.85m – 10M cells. 48
Figure 6.16 Velocity magnitude evolution with different time-steps at Z=5.85m – 2.4M cells 48
Figure 6.17 49
Figure 6.18 Velocity magnitude evolution. 50
Figure 6.19 Velocity magnitude and Y-velocity evolution – ZX plane. . . 51
Figure 6.20 Velocity magnitude profile on a horizontal line – $Z = 5.85$m . 51
Figure 6.21 Velocity magnitude evolution. 53
Figure 6.22 Velocity magnitude and Y-velocity evolution – ZX plane. . . 53
Figure 6.23 Velocity magnitude profile on a horizontal line – $Z = 5.85$m . 54
Figure 6.24 Z-velocity percentage distribution. 55
Figure 6.25 3D path-lines coloured by velocity magnitude. 56
Figure 6.26 Velocity trend as a function of the number of cells. 57
Figure 6.27 Polonium rate on horizontal lines – ZX plane 58
Figure 6.28 Vertical polonium distribution in the Fiducial Volume. 59
Figure 6.29 3D calculated ^{210}Po rate. 59

List of Tables

Table 4.1 Geometrical parameters of the 2D computational grids. 20
Table 4.2 Geometrical parameters of the 3D computational grids. 21
Table 4.3 Numerical discretization schemes. 25
Table 4.4 Under-relaxation factors. 25
Table 4.5 Fixed properties for the pseudocumene. 26

Table 5.1 Geometry and fluid-dynamics results of the 2D simulations. . . 35

Table 6.1 Time characteristics of the basic simulations. 38
Table 6.2 Geometry and fluid-dynamics results of the simulations. 43
Table 6.3 Temporal information of the test 2. 45
Table 6.4 Geometry and fluid-dynamics results of the simulations. 52
Table 6.5 Geometry and fluid-dynamics results of the simulations. 55
Table 6.6 Geometrical prevision for the possible future computational grids. 57

Introduction

The present work is a study inserted in the wider environment of the Borexino experiment. Borexino is a neutrinos detector located in the Laboratori Nazionali del Gran Sasso, Italy. It is running since May 2007 but, considering the R&D phase, the whole experiment saw at least three decades of efforts.
Important results have been reached until now. By the way, problems related to the radio-purity of the scintillator fluid are still permanent. The flows of neutrinos generated by the CNO-cycle in the Sun can be only detected if the suppression of the ^{210}Bi and ^{210}Po backgrounds is accomplished [1]. This thesis is clearly approaching the question from a thermo-fluid dynamic point of view. The main target is the generation of a model able to reproduce the movements of the fluid contained in the detector. This way, also the motion and the concentration of the contaminants could be directly appreciated. The focus is then posed on the polonium distribution.
Having such a reliable tool can afterwards be useful for the opposite intent: change the external thermal condition in order to finally reduce the contaminants.

The work has been completed thanks to the computational resources of the Polimi CFDLab, in the Bovisa campus. The Ph.D. Eng. Valentino Di Marcello, who works at the laboratories in the Gran Sasso, supported all the phases of the project.
Throughout the chapters is given a deep description of the problem and of the followed passages made to arrive at the final model. A brief overview is now listed.

Chapter 1 introduces the details on the Borexino experiment, from the neutrinos detection strategy to the structural design of the detector. Moreover, the background stability argument is discussed. Finally, the thermal monitoring & management system is described.
Chapter 2 focuses on the thermal environment in which Borexino is inserted and on the previous simulations. After this chapter, the reader will gain a total understanding of the system.

In **Chapter 3**, the governing equations characterising the mathematical problem are reviewed. **Chapter 4** instead explains how the numerical model is build-up. Information about the meshes generation, the initial and boundary conditions and the various models setups are given.

The results are split. The bi-dimensional and tri-dimensional simulations are respectively treated in **Chapter 5** and **Chapter 6**. Both the sections contain the fluid-dynamic studies and the evaluation, compared to the experimental data, of the concentration of ^{210}Po in the inner part of the detector.

The relation between the 2D and 3D results has a central role in the global analysis. It can produce a mutual feedback between the two approaches.

Chapter 1

Borexino detector and background stability problem

The present chapter is focused on the general description of the Borexino detector. The operating goals of the experiment are presented and the main problem of the background stability is introduced. Finally, an accurate characterisation of the thermal monitoring & management system is given.

1.1 Borexino detector

Borexino detector is a large volume ultra-pure liquid scintillator located in the Hall C of the Laboratori Nazionali del Gran Sasso (Italy). This particular location permits to have 1400m of shielding in every direction provided by the carbonate rocks of the mountain. The goal of the experiment is the measurement of sub-MeV (low energy) solar neutrinos via neutrino-election scattering. The detector is running since 2007, except for short maintenance and purification periods, and it has given extraordinary results, see [1], [2] and [3].

1.1.1 Neutrinos detection

The neutrino is one of the most negligible pieces of matter. It was first postulated by Pauli in 1931. Neutrinos are produced at the center of the Earth, in the Sun and even in supernovae; their study can tell us a lot about the conditions in those places. Its mass is less than one-millionth that of the electron while in the Standard Model it is supposed to be zero. Also for this reason the neutrino became one of the most studied particle in the last decades.

Elastic *νe* scattering is the principal reaction which permits Borexino to detect neutrinos. The particles themselves are not seen directly, but they pass some of the kinetic energy to electrons. Electrons are slowed down by ionizing interactions with the surrounding fluid. This process is able to electronically excite other molecules which will emit a light that is observed by a set of photomultipliers (PMTs); this is the reason why Borexino is defined as a scintillation detector [4].

The low energy neutrino detection is possible because of the liquid nature of the scintillator at ambient temperature. This provides very low solubility of ions and metal impurities, and gives the possibility to purify the material. However, the most important aspect in order to measure such a low neutrino flux is a formidable requirement of radio-purity inside the scintillator and in the whole structure. The radioactivity of the inner part should be low enough compared to the expected neutrino signal. A prototype of Borexino, the Counting Test Facility (CTF), has been previously built in order to measure the radioactive contamination of a liquid scintillator and it played a fundamental role in the R&D phase.

Furthermore, also the γ radiation coming from the external rocks and directed to the center of the scintillator volume present stringent requirements [5].

Neutrinos detection anyway exceeds the field of interest of this thesis. More accurate information can be found in [6].

1.1.2 Detector design

The hardware of Borexino is based on the principle of graded shielding, which practically means an onion-like design for the structures of the detector. This kind of choice is driven by the necessity of reaching a sufficiently low number of radioactive background events in the inner part. In fact, going towards the center, every region should exhibit lower levels of radioactive contaminants.

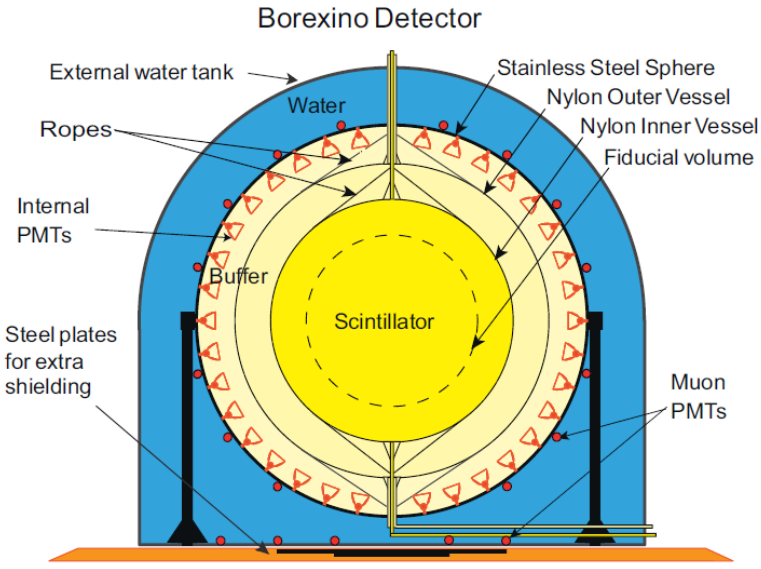

Figure 1.1. Schematic drawing of the Borexino detector

The core of the detector is the Inner Vessel (IV), a sphere of 8.4m in diameter which contains 273 tons of scintillator fluid. This liquid solution consists in PC (pseudocumene, $C_6H_3(CH_3)_3$) as a solvent and PPO (C_15H_11NO) as a solute at a concentration of 1.5 g/l. This solution presents high scintillation yield, high light transparency and fast decay time. Pseudocumene is a hydrocarbon formed by one benzene ring and three methyl groups. PPO instead in a heteroatomic five-membered

ring with two benzene rings; this benzene rings are crucial for the scintillation.

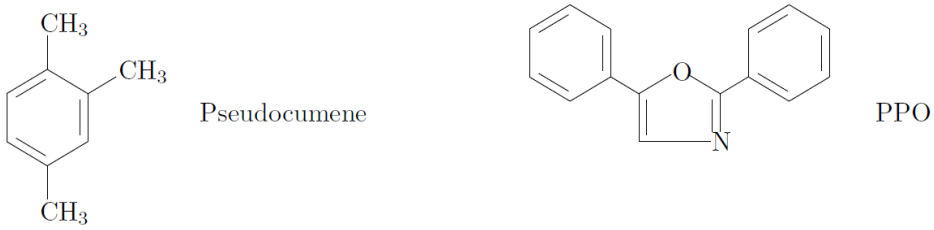

Figure 1.2. PC and PPO molecules

Inside the IV, another smaller spherical volume of 6m diameter is identified; this is not delimited by a physical boundary. The region is named Fiducial Volume (FV) and it is where neutrinos measurements are taken. Obviously this must be the purest zone of the whole detector.

The IV is made of a 125 μm thick Nylon-6 structure. Enclosing this sphere there is another Nylon-6 film (Outer Vessel) of 10.9m diameter which determines two different regions: the Inner Buffer and the Outer Buffer. The first, closer to the IV, contains 319 tons of buffer fluid. The second is filled with further 586 tons of the same fluid, a mixture of PC and few (5 g/l) DMP (dimethylphthalate, $C_6H_4(COOCH_3)_2$). This solution is chemically compatible with nylon, has a low light absorption and is relatively cheap. The possibility of scintillator solution leaking outside in the buffer (and vice versa) has been considered. During the whole lifetime of the experiment a 1.5m^3 of fluid exchange, in either directions, could occur. Anyway, this is not affecting the results in a relevant way [7].
In reality, after one year of experiment, a leakage was found; from a spot in the upper part of the IV a flux of 1.5m^3/month towards the buffer was changing the IV spherical shape. The DMP concentration in the buffer was decreased from 5 g/l to 2 g/l so to reduce the flux. Instead, in order to restore the shape, new scintillator fluid has been inserted inside the IV in two different moments, October 2008 and June 2009 [8].
The nylon structures are so thin because the buffer and the scintillator fluids have practically identical physical properties. Densities in particular differ by one time per thousand [9]. These structures are attached with Synthetic Texitle ropes to a rigid Stainless Steel Sphere (SSS).

The SSS has the fundamental role to sustain, on its inner surface, the 2212 photo-multipliers committed to the collection of the scintillation light. All but 384 PMTs are equipped with light concentrators, designed to reject photons that are not coming from the FV. The SSS, 13.7m diameter and 8mm thick, is supported by 20 steel legs and it is fully contained by an outer tank filled by 1000 tons of high-purity water. This final layer has the role of both detecting high-energy muons passing through the SSS and decreasing the γ rays coming from the surroundings of Borexino.
Finally, on the floor beneath the SSS, two steel plates are present, an additional shielding from rocks radiation [4].

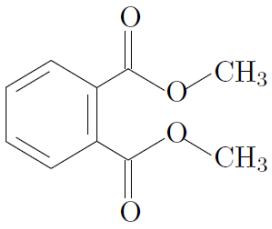

Figure 1.3. DMP molecule

More information regarding the instrumentation employed in the detector is presented in the next section 1.2.

1.2 Background stability

Borexino expects to observe 0.35 neutrino events per day per ton of scintillator liquid. Because there are so few events it is desirable to have a total background event rate that is very small; basically, solar neutrino events cannot be distinguished from background events. The rate of background events that are not identified and removed through cuts during analysis should be less than the neutrino rate. The signal to noise ratio should be S/N>1; the only way to increase this number is to reduce the background.
Enormous efforts are put into dealing with the large number of radioactive isotopes that decay with energies in or above the region of interest.

1.2.1 External background

With external background is intended all the radiation originated in the outside environment or in the material within the detector but still out of the FV. Some of the backgrounds are easily absorbed, while others, like muons, penetrate the shielding and must be subtracted from the collected data.

Ambient activity levels can vary from earth's average. Neutron flux from the rock walls of the Hall C was measured to be $3.8\text{n/cm}^2\text{/s}$. γ flux is also present and almost completely absorbed by the water shield.

Muons that pass through the inner vessel produce scintillation light. Their presence is a problem for Borexino even though they are efficiently tagged by the muon veto with an efficiency of better than 99.98%. Around 5000 muons per day enter the SSS and some of them interact with nuclei in the scintillator. Muons can break apart nuclei producing radioactive isotopes [6]. In this way muon-induced neutrons propagate rapidly through the scintillator but at the same time they can be detected because of the presence of a parent muon which crossed the boundary and deposited a large amount of energy [8].

Material activity of the materials used to shield the detector is also relevant and was carefully considered in the design phase. Again, particular concern were the γ emitters. It has been not easy to measure and catalogue the impurities in every material.
Some backgrounds are also produced by PMTs and the only way to reduce their impact in the FV was to move them to larger radius and so enlarge the SSS [6]. The contribution of the light source system is approximately 1/5 of that from the PMTs in the whole scintillator volume for events above 250 keV, but it drops to about 10^4 of it in the 100-ton expected fiducial volume. The radioactivity of the system is thus acceptable [9].

1.2.2 Internal background

Internal backgrounds include any decay that occurs inside the fiducial volume. They are a result of the presence of radioactive isotopes in the liquid scintillator. By eliminating sources of radioactive background in the target mass the rare interactions of neutrinos will become visible.
One of the most challenging technical issues facing Borexino is the identification and elimination of the impurities in the scintillator. Anyway, there is a vast quantity of data regarding naturally occurring isotopes; the knowledge of how each isotope decays, the energies of those decays, and their half lives facilitates the identification.
The rate of background events from radioactive isotopes produced in the detector is given by the number of atoms in the detector divided by their mean life. Isotopes with mean lives much longer than the duration of the experiment will produce a background that is nearly constant in time.

Radioactive isotopes in nature are part of a decay chain. The two most common are the ^{238}U and ^{232}Th chains. If either of these elements is present in the scintillator they will produce a series of radioactive decays that will produce a background in the detector. The concentrations of elements in the decay chains can be converted to an initial equivalent amount of ^{238}U or ^{232}Th. This gives a standard way of describing the concentration of all elements in the chain. However some factors can break this equilibrium. This is frequently done by the noble gas radon. Once equilibrium has been broken, describing the chain in this way is no longer valid [6].

^{14}C

^{14}C is by far the largest Borexino background and it determines the detector low-energy threshold. In order to reduce the levels of contamination, the Borexino scintillator is derived from petroleum from deep underground where the levels of ^{14}C are reduced by roughly a factor of a million compared with the usual values in organic materials. The 156 keV ^{14}C end-point is low enough that it is possible to safely fit the energy spectrum beyond it and keep high sensitivity to the neutrinos detection.

^{210}Po

^{210}Po is after ^{14}C the most abundant component of the detected spectrum. The strong ionisation quenching of the scintillator brings its spectrum within the neutrinos energy region. Even though it is a direct daughter of ^{210}Bi, the rate of ^{210}Po was about

800 times higher than that of ^{210}Bi at the start of data taking. Its energy region shows a significant non-uniformity, further perturbed by the detector operations and mixing [3]. A relevant feature which gave credence to the convective fluid movement was a low-^{210}Po volume that rose from the bottom to the top of the IV between August and November 2014. This phenomenon can be seen as polonium falling along the periphery of the vessel and afterwards levitating through the middle of the IV. Indeed, the problem is that the combined bismuth+polonium levels have been oscillating in a non-predictable fashion even though spectra fitting has been attempted for different periods [10]. *Thus, it is clear that the understanding and the prediction of the fluid-dynamic of the scintillator fluid inside the IV is a fundamental task in order to increase the detection quality of Borexino.*

^{222}Rn

The detector exploits the nylon vessels as a barrier to prevent radon from reaching the FV. The effectiveness of the barrier is determined by the reduction of the radon concentration across a thin nylon membrane. Radon properties are typical of a noble gas, being essentially non-reactive and having a large diffusion constant making it highly mobile. Its diffusion is governed by Fick's Law

$$\overrightarrow{\Phi} = -D\nabla\rho \tag{1.1}$$

where $\overrightarrow{\Phi}$ is the flux, D is the diffusion constant, and ρ is the density of radon. This can be after combined with the continuity equation

$$\nabla \cdot \overrightarrow{\Phi} = -\frac{\partial\rho}{\partial t} \tag{1.2}$$

Finally, to be complete, a source term has to be inserted due to the radium decay, and a loss term as well due to the radon decay itself

$$\frac{\partial\rho}{\partial t} = D\nabla^2\rho - \lambda_0\rho + A_{Rn} \tag{1.3}$$

where λ_0 is the decay constant of radon.
A lot of effort has been put into understanding and reducing radon contamination in Borexino. Moreover, radium embedded in steel also produces radon that can emanate from the surface [6].

Other dangerous background elements are ^{40}K, ^{85}Kr and ^{39}Ar, all β emitters [9].

1.3 Borexino Thermal Monitoring & Management System (BTMMS)

Beside a purification campaign thought to tackle the problem from the root, another idea has been developed in order to solve the issue concerning the fluctuations of the backgrounds mentioned in the previous section. The Borexino Collaboration decided to measure the temperature profiles inside and outside the detector, as well as thermally insulate it from the ambient temperature excursions of the Hall C. This has been done between late 2014 and the early 2016.

1.3.1 Latitudinal Temperature Probes System (LTPS)

LTPS is designed as a vertical profile monitoring system. Its goal is to allow for a better understanding of temperature-driven background fluctuations. It is divided in three different sets of probes which have the scope of measure temperatures on two sides, south and north directions respectively.
The probes can be summarised as:

- 28 internal probes located next to the PMTs cable ports on top of the detector, from 0.5m outside the SSS, up to 0.5m inside the Outer Vessel;
- 20 external probes located on the external surface of the WT, complemented by 6 probes located in a T-shaped service tunnel under the detector;
- 6 external probes located on the upper dome of the WT, 1 inside the calibration clean-room located over Borexino, as well as several probes for exterior ambient air readings.

The output of this sensors is a voltage differential then converted by a C++ program to temperatures according to empirically-determined calibration functions. The internal sensors are easily accessible for removal, replacement or relocation.
The presence of probes specifically on the top and on the bottom is due to the existence of a positive gradient (higher temperatures on top, lower temperatures on the bottom) in Borexino; a precise knowledge of this gradient is paramount to keep good stability conditions and minimise internal currents.

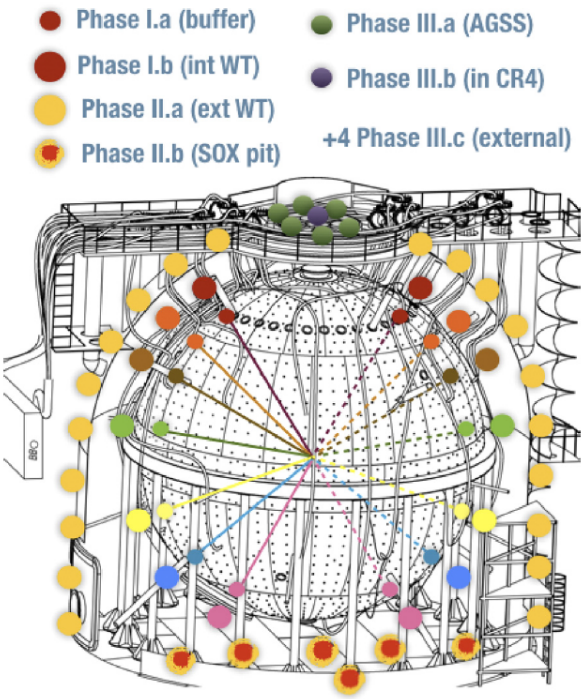

Figure 1.4. LTPS probes positions. Division by phase of installation.

1.3.2 Thermal Insulation System (TIS)

TIS efficiently increases the thermal resistance of the largest boundary of Borexino, the water tank. It consists of a 20cm thick double layer of mineral wool material which covers the full surface. This material has a low conductivity value of $\approx$ 0.03-0.04 $W/m \cdot K$.
Insulation started by the main surface, from the bottom up. Approximate $> 1000\text{m}^2$ of detector surface were insulated, including the organ pipes through which the PMTs cables enter the tank toward the SSS.

Figure 1.5. Sample of the TIS material

1.3.3 Active Gradient Stabilisation System (AGSS)

AGSS consists of twelve independent water loop circuits made by 14mm diameter copper serpentine tubing. It was installed before covering the WT with the TIS. It is designed with the scope of avoiding possible transient, first of all the increase in thermal gradient between top and bottom, which can affect fluid stability. 3 m^3/h of heated water are pumped through the tubes, from the upper part to the lowest, in order to provide constant temperatures ($\pm$ 0.1°C accurate controller) in the region of the system. This region is close to the topmost part of the detector and it is quite small compared to the total area of the tank [11].

Thanks to the operation of the AGSS and the collected data from the LTPS has been discovered that one temperature sensor is in a wrong position. In particular the probe number 4 on the south side of the detector and 0.5m outside the SSS (inside the water tank) is in a lower location. This sensor (s4) should be close to the middle plane, slightly higher, at a vertical position of 8.18m from the ground. Recently its position has been estimated around an height of 6m from the ground.
The set of probes in which s4 is contained is particularly relevant for the present work because the collected data are employed as an input for the CFD simulations, see paragraph 2.2.2. The position uncertainty of this sensor can affect the data analysis and consequently also the fluid-dynamics studies.

Chapter 2

Borexino thermal environment and previous simulations

This chapter illustrates the thermal conditions the detector is normally facing. In addition, the only conductive and convective Computational Fluid Dynamics (CFD) models developed in the previous works are presented.
It is then shown the employment of the sensors data and their importance is underlined. Finally, after a brief consideration on the Rayleigh number range of operation for the present work, the idea of the convective Water Ring model is introduced.

2.1 Borexino thermal evolution

It is now time to introduce the thermal environment in which Borexino is inserted and focus on the application of the experimental results given by the BTMMS. It is crucial to understand the temperature trend and the asymmetries characterising the system.

The temperature of the air in the Hall C is generally oscillating during the year. This air is in contact with the exterior part of the water tank and, obviously, affects its thermal behaviour. The annual average surface temperature of the WT is contained in the range of 286K - 290K [11]. Such a variation influences the internal temperature of the fluids in the scintillator volume. Thanks to the probes of the LTPS it has been possible to monitor this internal temperature in precise spots, see figure 1.4.

There are two main particularities which generate convective flows in the pseudocumene and are the cause of the internal currents mentioned in the first chapter.
The first asymmetry in the detector temperature distribution is the **top-bottom gradient**. LTPS data taking begun in 2014, since then the gradient magnitude varied from a minimum value of ≈2.2°C to a maximum of ≈5.2°C, reached in July 2016.
Borexino lifetime has been divided in three periods: the *uninsulated* period, before the TIS installation, a *transient* phase, during the installation and the *fully-insulated* period, after the work was completed. The detector inner temperature saw a rapid increase in the middle period, followed by a decrease and stabilisation once the TIS was totally located. This insulation system ensured the influence of the external air

temperature to be less effective. The first six months of the *fully-insulated* period showed significant stability in all areas of the detector.
The AGSS operation, started in December 2016, had the aim of maintaining the top temperature at a constant value of ≈17.5°C, always higher than the environment condition. This way, the situation could be kept under control, avoiding de-stabilizing events for the background IV distribution.

The other important feature is the asymmetry **between the North and South** sides. This irregular distribution is due to the slight different external conditions each side is subjected to, to uneven temperatures as well as seasonal upsets. The temperature difference could reach values of ≈0.1°C and it is function of the latitude. It the next sections it is possible to see how deeply this asymmetry can affect the internal fluid dynamics.
Thus, the detector temperature profile exhibits a vertical stratification. On the topmost region temperatures are more uniform, whereas in the bottom part the gradient is sharper and therefore the stratification presents more isotherms [11].

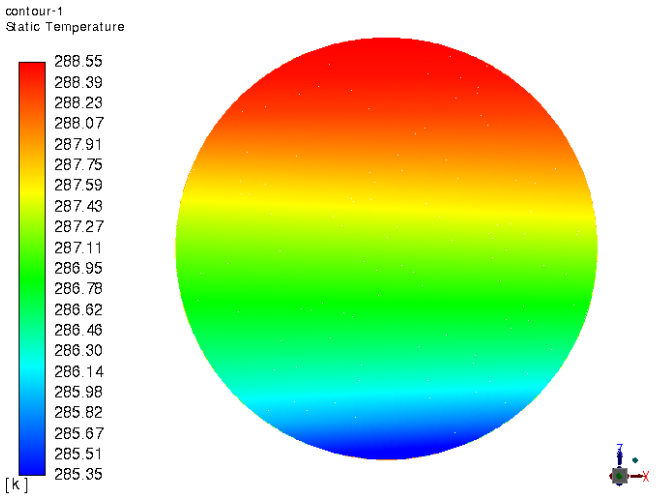

Figure 2.1. Initial temperature distribution for the IV. Picture taken from the 3D convective simulation of the IV (see below) of February 2017.

This is a particular situation of natural convection driven by really small asymmetries. It means that every little variation in temperature BCs and every singularity of the employed model (time step, internal mesh, boundary layer) could bring to differences in the final solution.

2.2 Previous CFD models and simulations

Beside the installation of the BTMMS, in order to better understand the thermal and fluidodynamic development of the detector, several CFD models have been implemented. To do this, the simulation package *ANSYS*® FLUENT™(v. 16,17 and

19.1) has been exploited thanks to the computing resources of the CFDLab in the Energy Department of Politecnico di Milano, Bovisa.

Starting from the LTPS temperature data collected during the experiment, simulations has been carried out; boundary conditions (BCs) set up is explained in the next chapter. The outcome could afterwards help deciding the following directives for the operation of the AGSS. The purpose was, and remains, to ensure a higher stability in background shifting and predict its behaviour.
The simulations are basically divided in two types: only conductive and convective. The purpose of the first was to gain the precision of the model in calculating temperatures and heat fluxes both in the fluids and in the structures. The second, instead, were more focused on determining the fluid movements inside the IV. A lot of cases has been run with the target of checking the numerical noise, the influence of different BCs and simulating the presence of the AGSS.
A brief overview of the simulations is listed below.

- Bi-dimensional only conductive simulations;
- Three-dimensional only conductive simulations;
- SSS convective bi-dimensional simulations;
- *Water Ring* and IV convective bi-dimensional simulations.

2.2.1 Rayleigh number range of operation

Before starting the convective simulations several benchmarking cases have been implemented with the scope of characterising FLUENT capability in reproducing physical well studied cases in literature [12] [13]. The idea was to reproduce a system as similar to Borexino as possible; so, this cases were studying the convective behaviour in cylindrical systems with a bi-dimensional schematization.
The temperatures were chosen to lie inside the range of Rayleigh number (Ra) concerning Borexino. This dimensionless parameter contains information about the convective/conductive nature of the fluid dynamics. Rayleigh number is usually defined as the quotient multiplying Grashof number (Gr) and Prandtl number (Pr):

$$Ra = \frac{\beta \Delta T g L^3}{\nu^2} Pr \tag{2.1}$$

where $\beta[K^{-1}]$ is the thermal expansion coefficient, $g[m/s^2]$ is the gravitational field, $\nu[m^4/s^2]$ is the kinematic viscosity, $\Delta T[K]$ is the temperature difference in the characteristic lengthscale of the system and L [m] is the characteristic lengthscale itself. Pr quantifies the quotient between the momentum and thermal diffusivity.
The ΔT was chosen as the temperature upsets which cause the isotherm displacement and not the overall gradient between top and bottom; so, $\Delta T = 0.1K$. Thus, considering the radius of the IV, it results a characteristic length of $L \approx 0.17$m separating each $0.1K$ isotherm.
Finally, taking the values of $\beta_{PC} \approx 10^{-3}K^{-1}$, $\nu_{PC} \approx 7 \cdot 10^{-7}m^4/s^2$ and $Pr = 7.78$, Rayleigh number range for Borexino application has been estimated $Ra \in$

$[\mathcal{O}(10^7), \mathcal{O}(10^8)]$. Keeping in mind that we are not really working with a linearly-stratified fluid, this range has to be enlarged to $Ra \in [\mathcal{O}(10^6), \mathcal{O}(10^9)]$.
It is important to underline that from this brief calculation it is possible to infer that the system presents a situation of *laminar flow* in natural convection. This is extremely important for determining a suitable model setup and the software options.

2.2.2 *Water Ring* and *IV* convective bi-dimensional simulations

The coupled bi-dimensional convective simulations of the Water Ring (*WR*) and the Inner Vessel are particularly significant because they represent the connection between previous works and the present.

This section is thought to give an explanation of the principal of operation of the Water Ring model; the various IV models are deeply and carefully treated in the next chapters.
The main target of the *WR* model is to propagate and faithfully reproduce the BCs in the inner part of the detector. These BCs are built up from the LTPS data through an interpolation process; it is clear that these temperatures are varying in time during the simulated period, usually one month.
The mesh itself presents two fluid regions, one for water and the other for the internal pseudocumene. Moreover, all the real surfaces dividing the fluids and described in section 1.1.2 are modelled.

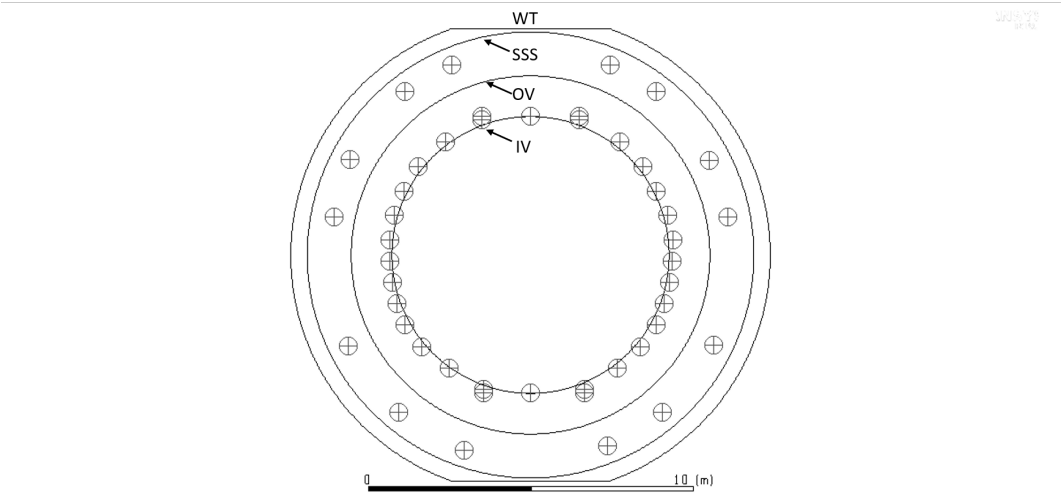

Figure 2.2. Water Ring model structure.

It has been proved that Water Ring model is a valid benchmark for the thermal transport and quite faithful for the temperature evolution [11]. The output data have been compared to the LTPS probes inside the Outer Buffer and the difference in temperatures is less than ± 0.2°C. Anyway, the model is not a benchmark for the fluid

transport. It produces unrealistic currents or fully numerical flow patterns. This is the reason why a separate IV model is needed in order to study and characterise the internal fluid dynamics.

Thus, as a result of the *WR* simulation, it is possible to extract the temperatures from previously located spots at the border of the Inner Vessel (see figure 2.2). These values are consequently employed as BCs for the IV models. From the previous works, the bi-dimensional modelling of the Inner Vessel revealed stratified horizontal flows in the internal bulk. This behaviour will be confirmed by the present study.

No heat transfer on the structures is computed since the physical boundaries are modelled with zero-thickness. The walls simply represent a division between the various inner regions of the detector. While the SSS is in contact with water and pseudocumene at its borders, the other nylon films are only surrounded by scintillator fluid.

Chapter 3

Governing equations for the mathematical models

In this third and short chapter the set of governing equation which mathematically characterises the problem is given.
In the first part is explained how the fluid-dynamic behaviour is treated. This model is afterwards implemented in FLUENT.
In the second section instead, it is described the equation used to predict the Polonium mass transfer in COMSOL Multiphysics.

3.1 Pseudocumene fluid-dynamic model

The chosen way to describe the flow field of the pseudocumene inside the IV are the mass, momentum and energy conservation equations (*Navier-Stokes* equations) for an incompressible Newtonian fluid. Viscosity and density are generally considered constant.
The system of equations takes the form:

$$\frac{\partial \rho}{\partial t} + \nabla \cdot (\rho \mathbf{u}) = 0 \tag{3.1}$$

$$\frac{\partial (\rho \mathbf{u})}{\partial t} + \nabla \cdot (\rho \mathbf{u}\mathbf{u}) = -\nabla p + \nabla \cdot \overline{\overline{\tau}} + \overline{\rho}\mathbf{g} \tag{3.2}$$

$$\frac{\partial (\rho E)}{\partial t} + \nabla \cdot [(\rho E + p)\mathbf{u}] = \nabla \cdot [(\overline{\overline{\tau}} \cdot \mathbf{u}) + k\nabla T] \tag{3.3}$$

Where ρ, $\mathbf{u}$ and E are the density, the velocity vector and the energy, respectively. p is the static pressure, $\overline{\rho}\mathbf{g}$ the gravitational body force, k the thermal conductivity and $\overline{\overline{\tau}}$ the stress tensor.
The basic idea of these transport equations is to have the *rate of change* term and the *convective* term on the left and the *diffusive* and *source* term on the right-hand side. The resolution method and the chosen property values are presented in the following chapter.

3.1.1 Boussinesq approximation

An important approximation has to be inserted since the problem is concerning natural convection. The Boussinesq approximation models the fluid density as a function of temperature. So, the fluid density is considered as variable in the *body force* term and is here linearized. This can only be done when the density variations are small.

$$\overline{\rho}\mathbf{g} = (\rho - \rho_0)\mathbf{g} \simeq -\rho_0\beta(T - T_0)\mathbf{g} \tag{3.4}$$

$$\beta = -\frac{1}{\rho}(\frac{\partial\rho}{\partial T})_p \tag{3.5}$$

where β is the thermal expansion coefficient.
In this way it is possible to reduce the non-linearity of the governing equations. From a computational point of view, this kind of treatment provides faster convergence in respect to other temperature-dependent density formulations [14].
Easy to notice that the momentum and energy conservation equations (eq. 3.2 and 3.3) are strictly correlated by the temperature. Temperature asymmetries, in natural convection problems, are in fact the driving force of the fluid motion.

3.2 ^{210}Po mass transfer model

The polonium migration inside the Inner Vessel is modelled through a convection-diffusion equation. The model predicts only the ^{210}Po transfer, avoiding to consider its predictors (bismuth and lead). These other elements are considered much less mobile compared to the polonium and they cannot easily pass the nylon structure of the IV [15].

$$\frac{\partial C_{Po}}{\partial t} + \mathbf{u}\nabla C_{Po} = \nabla \cdot (D\nabla C_{Po}) - \lambda_{Po} C_{Po} \tag{3.6}$$

Where C_{Po} is the polonium concentration, D its diffusion coefficient, λ_{Po} the decay constant and $\mathbf{u}$ is the velocity vector. This vector is directly taken from the resolution of the Navier-Stokes equations previously mentioned. In such a way, it is possible to decouple the fluid-dynamic problem from the ^{210}Po transfer.

Chapter 4

2D and 3D numerical domains and models setup

In this forth chapter it is presented in detail the the structure of the CFD models previously mentioned. The target is to describe the whole numerical model development for the system.
Starting from the meshes description for the 2D and 3D cases, all the differences will be highlighted. Consequently, it is described the BCs formation procedure, from the LTPS data to the used interpolation. Furthermore, the chosen numerical model is shown. Finally, a brief paragraph on the 2D mass transfer model in COMSOL for the ^{210}Po prediction is present.

4.1 Mesh generation and geometrical model description

4.1.1 2D computational grids

It is important to underline that the 2D grid generation has been carried out in previous works. So, this section aspires to simply describe the taken choices.

The 2D model exhibits different geometrical simplifications in order to reduce the computational cost and time and to decrease the real number of elements of the detector. With this perspective, Borexino is designed as several concentric cylindrical domains (fig. 2.2).
The bi-dimensional computational grid used to discretize the domain is, depending by the precise position, a structured Cartesian or a polygonal/polyhedral grid. Preliminary mesh sensitivity analysis permitted to determine the mesh size Δx suitable for each geometry.

The Water Ring model, mentioned in section 2.2.2, presents a coarser discretization because its only aim is to reproduce the temperature map at the border of the IV. This particular model is composed by ≈118k hexahedral orthogonal cells with local refinements close to the walls [15].
On the other hand, the IV models show a more refined mesh with the scope of a full

and reliable characterisation of the internal fluid currents. Two different grids are employed for the analysis in the present work. The detailed information about the grids are stored below in table 4.1.
The usage of two distinct meshes gives the possibility to compare the obtained results and to gain some feedback concerning the differences between the two.

N° cells	Average cell size [m]	BL thickness [m]	Min orthogonal quality
270k	0.01447	-	0.2727
530k	0.01034	0.020	0.6905

Table 4.1. Geometrical parameters of the 2D computational grids.

The grids have a number of cells in the order of $\mathcal{O}(10^5)$. Easy to understand that the attempt is to double the cells between one case and the other.
The average cell size is simply obtained dividing the area to the number of cells. It can be also seen that the first mesh is characterised by an acceptable value of orthogonal quality while the second reaches a good one. Moreover, some observations should be done about the boundary layer thickness. With boundary layer thickness it is intended the length of all the layers of cells present at the border of the domain. These layers are intentionally structured to better compute the boundary thermo-fluid dynamic trend. It can be noticed that in the 270k cells mesh such a solution is not present (fig. 4.1a); it has been opted just for a local refinement. In the other mesh there are seven organised layers (fig. 4.1b) and their thickness amounts to 2cm; this choice turned out to be healthy for the behaviour understanding.

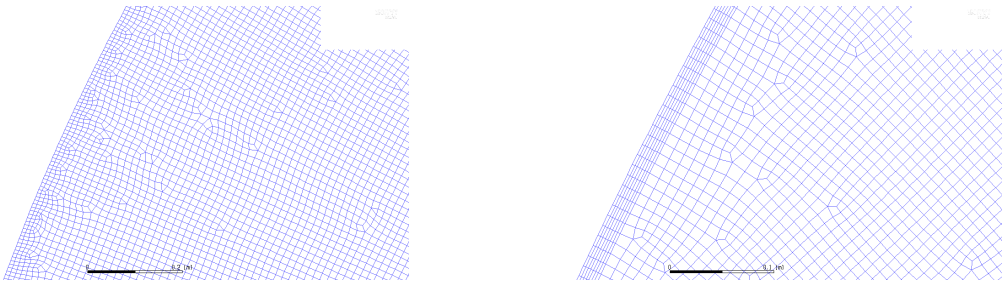

(a) 270k cells (b) 530k cells

Figure 4.1. Boundary layer comparison for the 2D cases.

4.1.2 3D computational grids

Differently from the 2D cases the generation of the 3D meshes have been developed in the present work. For this particular task has been always exploited the FLUENT package, in particular the FLUENT 3D meshing option.
The generation process started from a very simple sphere CAD model. This sphere has a diameter of 8.5m in order to reproduce the real dimensions of the IV. Once the CAD was imported it has been possible to define the minimum and maximum

cell size and the number of layers of the BL for each case. At the variation of the maximum cell size a different number of cells has been reached. All the geometrical parameters are summarised in table 4.2.

	N° of cells	Min cell size [m]	Max cell size [m]	BL thickness [m]	Min orthog. quality	Max skewness
Coarse	2.4M	0.018676	0.0615	0.0367	0.445	0.555
Fine	5M	0.018676	0.0475	0.0284	0.538	0.462
Very fine	10M	0.018676	0.03735	0.0222	0.4816	0.518
ΔBL	10.2M	0.018676	0.03735	0.02	0.4800	0.520
Extra fine	20M	0.018676	0.02950	0.02	0.4760	0.505

Table 4.2. Geometrical parameters of the 3D computational grids.

Again, the idea is to every time double the number of cells in order to have a comparison and to understand, through a sensitivity analysis, when the discretization is good enough. The number of elements is in the order of $\mathcal{O}(10^6)$. All the meshes have tridimensional polyhedral cells in the whole volume except for the external layers. Both values for orthogonal quality and skewness result acceptable in each case.
The grids have been generated in two different moments along the project evolution. At first, the three smallest meshes were built up; in a second moment, the generation has been completed with the addition of the biggest two. The substantial difference between the two groups is the BL structure. While in the fist case only the number of layers (6) has been imposed, in the second the intention was to reproduce in 3D the bi-dimensional layout which brought to satisfying results (see chapter 5). So, the 10.2M and 20M cells grids boast the presence of 7 layers with the smallest total thickness of 2cm. The BL thicknesses of the other specific cases are reported in table 4.2. The comparison can be appreciated in the figure below.

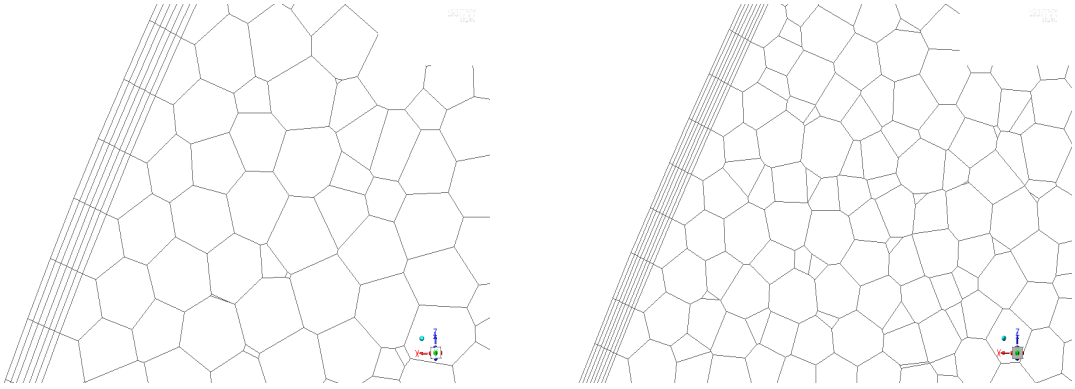

(a) 2.4 Millions of cells (b) 10.2 Millions of cells

Figure 4.2. Boundary layer meshes comparison.

The Z axis of the model is associated to the vertical one. The image compares the meshes from the views of the ZX vertical plane. The difference in dimensions is clear.

4.2 Initial and boundary conditions

It is now described how the data from LTPS are treated in order to generate the initial and the boundary conditions for the different cases. Some differences are present between the 2D and the 3D domains so they will be discussed separately.
The idea is to linearly interpolate the known values located in the precise positions. Doing that, we are assuming a smooth behaviour between the various spots.
It is essential to underline that the Water Ring simulation (section 2.2.2) is only computed in two dimensions. The output temperatures taken from thirty spots at the border of the Inner Vessel are later employed for generating the BCs of both the 2D and 3D only IV models.

4.2.1 Bi-dimensional case

The **initial conditions** are imposed through a linear interpolation. The domain is practically divided in rectangular sub-domains who's vertices are identified by the imposed temperature spots. The initial temperatures for all the points inside the smallest domains, with coordinates (x,y), are given by the interpolation function:

$$\begin{aligned} T(x,y) = \frac{1}{A}[(\Delta T(R_1) \cdot |x - x_0| + \Delta T(R_0) \cdot |x - x_1|)y + \\ + |x - x_0| \cdot (T_1 y_1 - T_2 y_0) + |x - x_1| \cdot (T_4 y_1 - T_3 y_0)] \end{aligned} \tag{4.1}$$

where A is the area of the rectangle, T_i, with $i = 1, 2, 3, 4$, are the temperatures of the vertices and $R_{0/1}$ are the vertical temperature gradients between the north and the south vertices respectively.

As the simulation proceeds in time, updated **boundary conditions** have to be provided.

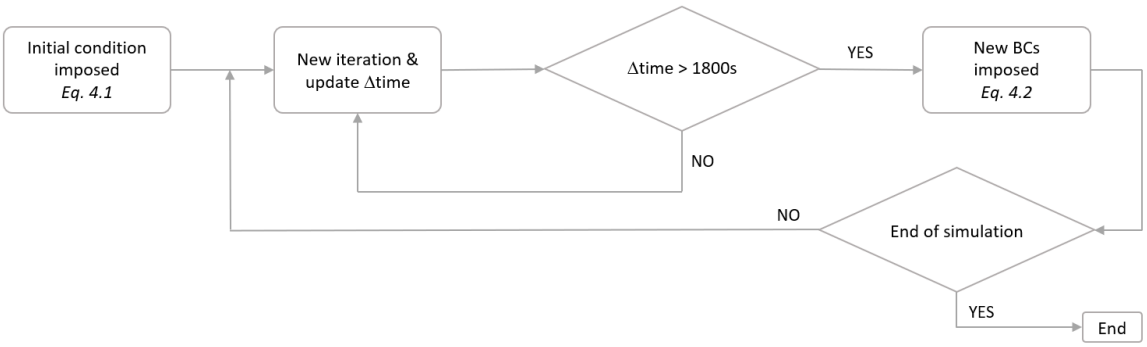

Figure 4.3. Simplified flow chart of the BCs imposition.

Every **1800s** of the simulated time, which is the standard time delay for the LTPS data acquisition, new temperatures are given at the border. To do this, the simulated time is constantly monitored through a loop; in the schematic flow chart $\Delta time$ represents the period passed after new conditions are given. Also in this case a linear

interpolation is exploited to guarantee a full and continuous profile in the boundary points. The temperatures are now function of time and the vertical position:

$$T_{N/S}(t,y) = \frac{1}{h_1^i - h_0^i}[T_{N/S}^{i+1}(t) \cdot (y - h_0^i) + T_{N/S}^{i}(t) \cdot (h_1^i - y)] \tag{4.2}$$

where $h_{0/1}$ are the heights of two adjacent known spots, i$\in$ [1,14] is the corresponding domain and N/S is the side.

This custom-made function (*time-evo*), which is internally developed by the Borexino collaboration, was verified to not generate deep enough changes to cause numerical divergences. For this reason it is also used for the tri-dimensional model.

4.2.2 Tri-dimensional case

In the 3D case it is not possible anymore to only execute a simple linear interpolation, the sub-domains are not rectangles but they have an unstructured shape.
The procedure consists in the formation of a mapping function able to transform an arbitrary quadrilateral into a square. This function will pass from physical to logical coordinates $(x, y) = f(l.m)$ where both l and $m \in [0, 1]$. In this way it is possible, and even in an easier way, to implement a linear interpolation [16].

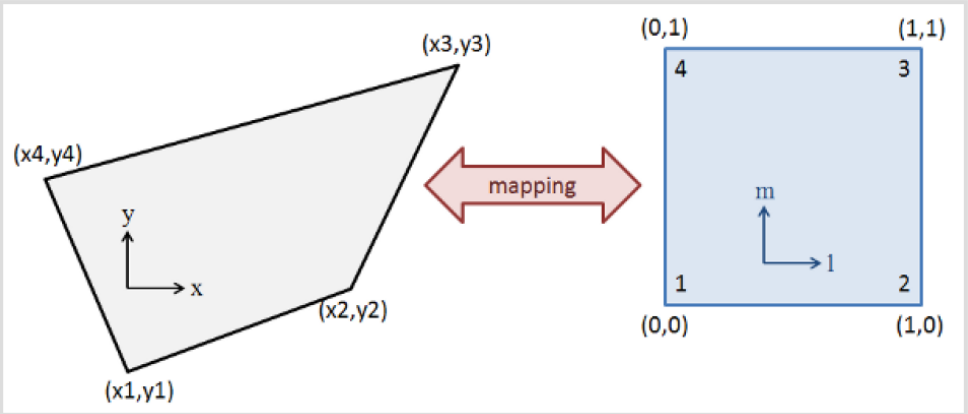

Figure 4.4. Mapping function schematic behaviour.

It is interesting to notice that, even if the result is a 3D temperature distribution, the interpolation anyway starts from bi-dimensional data; this is due to the location of the available LTPS probes, only present in the north and south sides. So, once the interpolation is done in two dimensions, the temperature pattern is applied both to the west and east 3D semi-spherical surfaces, in a fully symmetric way.

The mapping function is modelled as a bi-linear system:

$$x = \alpha_1 + \alpha_2 l + \alpha_3 m + \alpha_4 lm \tag{4.3}$$
$$y = \beta_1 + \beta_2 l + \beta_3 m + \beta_4 lm \tag{4.4}$$

Where the *alphas* and the *betas*, 4 for each domain, are obtained through the resolution of linear systems. These indices contain the information for every map to pass from physical to logical coordinates, and vice-versa.

Later, l is found inverting equation 4.3 and m from the consequently quadratic equation obtained from equation 4.4.

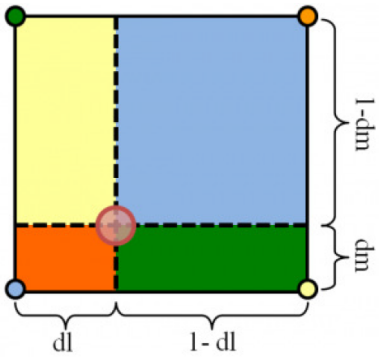

Figure 4.5. Area division for the linear interpolation in logical coordinates.

Since the area in logical coordinates is unity, temperature inside the domain is given simply by the sum of the vertices temperatures times the opposite area, see figure 4.5 for a better understanding.

$$T(m,l) = T_1(1-m)(1-l) + T_2 l(1-m) + T_3 ml + T_4 m(1-l) \tag{4.5}$$

The **boundary conditions** are always imposed thanks to the *time-evo* function. The flow chart seen in figure 4.3 is still valid. In this case the interpolation just explained is inserted in the function, eq. 4.2 is substituted by eq. 4.5. Also the *alphas* and the *betas* have to be added at the beginning. Clearly, the conditions are given in three dimensions.

4.3 Numerical model setup

The mathematical model presented in chapter 3 is implemented in the commercial software *ANSYS* FLUENT through a discretization in space and time.

4.3.1 Numerical algorithm

The algorithm employed for the equations resolutions is the coupling pressure-velocity **PISO algorithm**, which stands for Pressure Implicit with Splitting of Operations. It has been originally implemented as a non-iterative transient calculation procedure. With non-iterative is intended that it does not require iterations within a time level. Once the solution is reached inside the PISO process it is possible to pass directly at the following time step. To ensure good and accurate results a small time-step is required.
The PISO process presents internal loops and it can be considered as an extension of the SIMPLE method because it contains a further pressure correction equation. For this reason, an additional storage is asked but with the result of an efficient and faster method [17].

4.3.2 Discretization schemes

The discretization scheme is equally employed in 2D and 3D. In the tables below are reported the chosen solution methods.

Term	Scheme
Gradient	Least squares cell based
Pressure	Body force weighted
Momentum, Energy	Third order MUSCL
Transient	First order implicit

Table 4.3. Numerical discretization schemes.

As said, it is here evident that PISO is a transient implicit method. The choice of third order MUSCL scheme for momentum and energy equations grantees a highly accurate numerical solution.

To control the convergence and get a more stable solution some under-relaxation factors are set. All the other factors are fixed to one.

Correction	Factor
Pressure	0.3
Momentum	0.7

Table 4.4. Under-relaxation factors.

4.3.3 Time-step definition

The time-step (Δt) has been chosen in order to maintain the necessary accuracy and to satisfy the Courant-Friedrichs-Lewy (CFL) condition of CFL<1. Δt is defined considering the physical ΔT_p and the Fourier stability analysis.

$$\Delta t_p = \frac{\tau_0}{4} \approx \frac{L}{4\sqrt{\beta g L \Delta T_p}} \tag{4.6}$$

$$\Delta t_{Fo} = \frac{Fo(\Delta x)^2}{\alpha} \tag{4.7}$$

with τ_0 the time constant, L the characteristic length, Fo the Fourier number limited to $Fo = 0.1$, Δx the grid size and $\alpha = k/(\rho c_p)$ the numerical diffusivity. The maximum time-step for the different cases has been chosen [11]. The starting values for the 2D and 3D cases were 4.5s and 9s respectively. Considering that the simulated time is around 4 weeks, several hundreds of thousands of time-steps are needed.

Density	ρ	881	$[kg/m^3]$
Viscosity	μ	$1.112{\cdot}10^{-3}$	$[Kg/(m{\cdot}\ \mathrm{s})]$
Thermal expansion coeff.	β	$1.05{\cdot}10^{-3}$	$[K^{-1}]$

Table 4.5. Fixed properties for the pseudocumene.

4.3.4 Physical and thermal properties

The physical and thermal properties of the pseudocumene are listed in table 4.5. These are the values inserted in the model:
Density is specified at operating temperature of 288K. Viscosity is considered constant. The value for fluid thermal expansion coefficient β, which enter in the Boussinesq approximation, has been previously derived by density measurements at different temperatures.
The heat capacity and the thermal conductivity are instead given by user-define temperature dependent polynomial functions:

$$c_p = 1497.075 - 1.14419T + 0.00713T^2 \tag{4.8}$$

$$k = 0.203 - 2.72 \cdot 10^{-4}T + 8.52 \cdot 10^{-8}T^2 \tag{4.9}$$

Additionally, the default values for all the interested water properties in the *WR* simulation are taken.

4.4 ^{210}Po mass transfer model

The mathematical model presented in section 3.2 has been implemented in the commercial software COMSOL Multiphysics. This model can give a prediction of the ^{210}Po concentration inside the FV which can be compared with the experimental measurements.

The model contains several simplifications.
For the bi-dimensional cases the **spatial discretization** is taken equal to the FLUENT simulations. For the 3D model instead, a new less refined mesh with 1.1M of tetrahedral elements is directly crated in COMSOL.

The **velocity field** is taken from the CFD simulations. The velocity values are interpolated by the new software. Anyway, the mass transfer simulation setup maintains a constant velocity over time; this is giving reliable results since the temperatures at the border are experiencing very small variations and the situation is considered stable. The final solution can be considered as a picture of a ^{210}Po concentration evolution at a specific time.

The **boundary conditions** for the polonium concentration are then set and imposed to the equation 3.6. The concentration is assumed to be constant and uniform over the IV wall. Such a distribution comes from the idea that polonium uniformly migrates through the nylon film all around the vessel.

Chapter 5

Results of the 2D cases

The results, the computed analysis and the considerations about the various models are now presented. First, the 2D results are shown; consequently, another chapter about the 3D cases is inserted. Both parts contain a description of the fluid-dynamics and the results evolution; finally, an analysis of the ^{210}Po distribution prediction is added.
The simulated time is around 1 month, precisely 2'584'800s. The exploited LTPS data are related to the last week of January 2017 and the first three of *February 2017*. In the 2D case the total duration of the simulations (*WR* + IV model) is around 2 and a half weeks.

The main target of the 2D simulations is to characterise the fluid-dynamics of the IV pseudocumene and extract the velocity field. Beside this, a part of the investigation is focused on the problem with the unknown position of the temperature sensor s4, see section 1.3.2; two different temperature interpolations have been defined for the *Water Ring* simulation in order to impose the right profile. A complete list of the 2D analysis is now given:

- Comparison between the outputs of the three *WR* simulations: base case, 1° and 2° interpolation;
- study and comparison of the velocity field, output of the IV simulations with the coarse mesh: base case, 1° and 2° interpolation;
- study and comparison of the velocity field, output of the IV simulations with the fine mesh: only base case and 2° interpolation;
- overall analysis of the ^{210}Po distribution prediction.

So, the chapter is divided in three parts. First of all, the *WR* section. Second, the cell size sensitivity analysis on the IV model. Finally, the polonium distribution prediction.

5.1 *Water Ring* simulations

The *WR* simulation is the first step of the bi-dimensional analysis. Since the LTPS data of the probes 0.5m outside the SSS are employed as BCs, the set of probes

situated 0.5m *inside* the SSS are exploited as a comparative benchmark for the simulation outputs. From the results, temperature data are extrapolated in the exact position of the internal probes and the values are compared.
The procedure has been followed for three different cases:

- In the base case, the BCs are taken from the LTPS data without changes. s4 is thought to be at 8.18m from the ground;
- for the first interpolation, the value of the s4 temperature in the BCs has been linearly interpolated between the two adjacent probes. Its position is always assumed at 8.18m from the ground, as designed;
- in the second interpolation the vertical position of s4 has been set to be 6.28m from the ground and its value has been again linearly interpolated.

The simulations of the base case and the second interpolation have been carried out by Eng. Valentino Di Marcello (INFN) while the first interpolation and the whole post processing have been produced by the author of the present work.

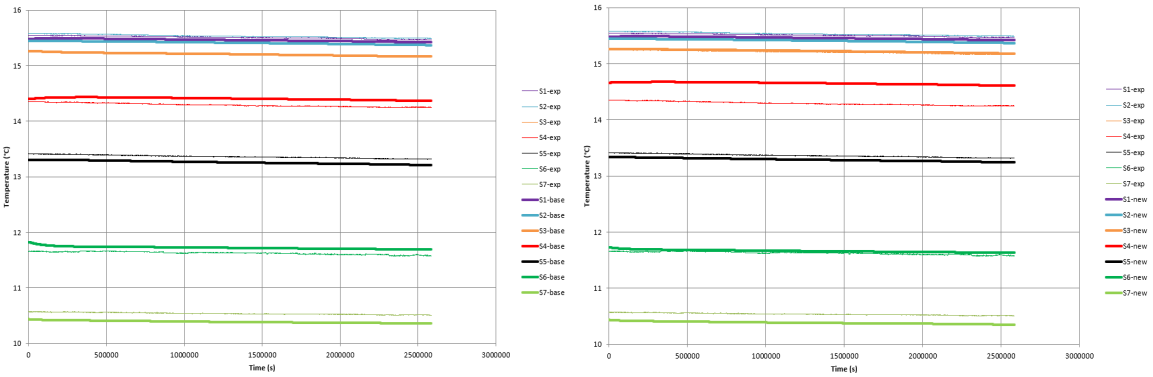

(a) Base case.

(b) 1° interpolation.

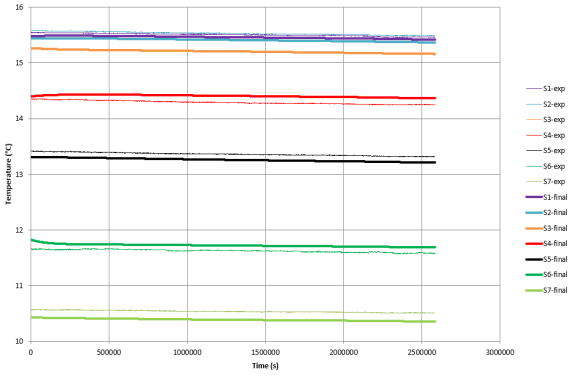

(c) 2° interpolation.

Figure 5.1. *Water Ring* simulation accuracy check – South side.

Attention has to be payed; the sensors reported in the figures are the internal ones. As said above, the simulation data are compared with the experimental data recorded in the same positions, which are represented by the thinner lines. To avoid

misunderstandings, from now on, the names of these internal probes are written in ***bold-italics***.

Looking at the figures it is clear that in the base case the temperatures are well reproduced in the upper part of the detector (***s1-s2-s3***) and weakly overestimated or underestimated, with an error which is around 0.15°C, in the lower area.

With the first interpolation the value of temperature in ***s4*** has clearly increased. The behaviour is consistent with the physics of the system because we are assuming for the external s4 a position that is higher than the real one. The topmost part always shows higher temperatures even if the temperature gradient is decreasing from the bottom to the top. This change has a repercussion also on the values of the probes ***s5*** and ***s6***; for these two the match with the data is improved. It is possible to infer that this would have an impact on the fluid-dynamics of a consistent part of the vessel.

Finally, with the second interpolation the situation seems to be very similar to the base case. In fact, the external s4 is now assumed to be closer to its real position. Small variations from the experimental data are anyway present.

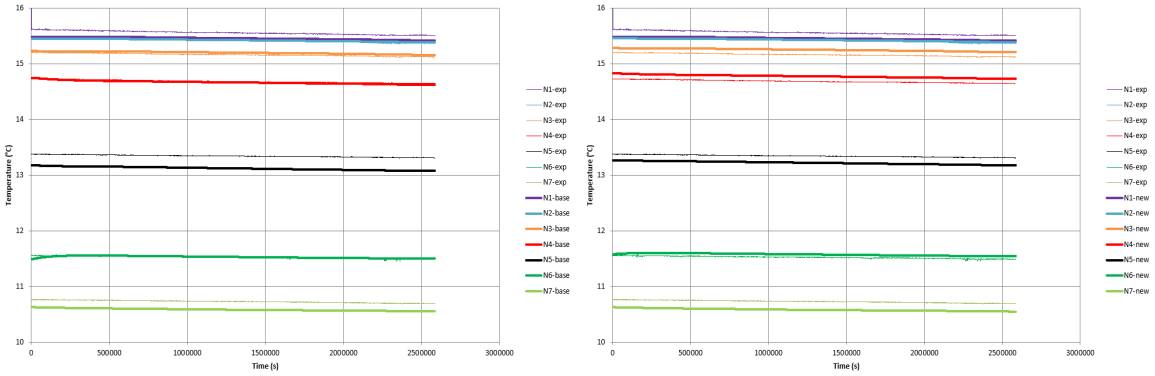

(a) Base case.

(b) 1° interpolation.

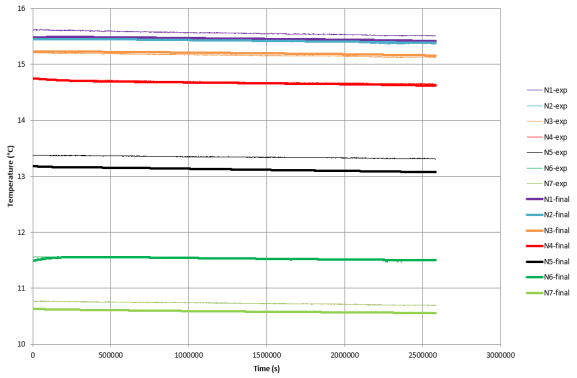

(c) 2° interpolation.

Figure 5.2. *Water Ring* simulation accuracy check – North side.

When it comes to the north side the trend is similar to the south side. Initially, a good reproduction is found for the bottom are; some irregularities are instead noticed in the other sensors, specifically for the internal ***n5*** .

From figure 5.2b it is possible to see how all the probes reach a higher temperature. The reason is the same of the south side situation. Here probably, the perturbation is

less strong than the previous case, but visible at every height.

In conclusion, the second interpolation still brings the results close to the base case.

Having seen these differences between the various *WR* model cases, it is now possible to introduce the results of the IV model simulations.

5.2 Cell size sensitivity analysis

Two models are studied in this paragraph. The goal is to appreciate the differences and pay attention on the resolutions of the results. First of all, a coarse computational grid is employed, with 270k cells. Afterwards, a refined mesh is exploited, the one with 530k cells. For each case, the mentioned BCs, outputs of the *WR* model, are imposed.

5.2.1 Coarse computational grid

This section contains the results of the first IV model, with a computational grid of 270k cells. The comparison is always done between the base case and the two interpolations, as explained right above. The main differences will be highlighted.

In order to characterise the evolution from the beginning, a strict monitoring of the velocities has been computed. This is the only analysis carried out for the base case solely. 21 points have been created in order to extract the velocity magnitudes, see figure 5.3b. For the first part of the simulation, every 1000s data has been saved. The result can be seen in the following image.

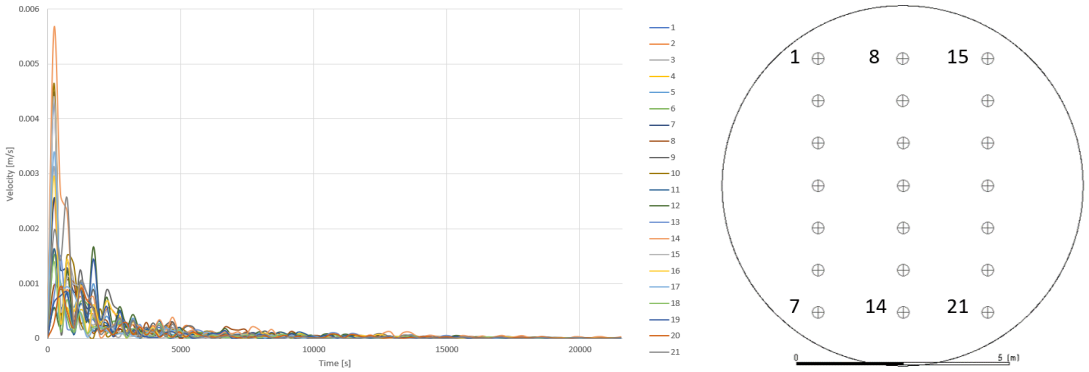

(a) Initial velocity magnitude evolution – Base case.

(b) Monitoring points.

Figure 5.3

The velocities, starting from a default value of $1 \cdot 10^{-10}$ m/s, rapidly increase and reach a peak after approximately 1000s of simulations. The initial order of magnitude is $\mathcal{O}(10^{-3})$ m/s. Thus, the trend shows a fast decrease until a stable situation is found around 20000s ($\approx$ 6 hours). Small fluctuations are continuously present. The behaviour is comparable for the majority of the points.

The **temperature** distribution confirms the isotherms stratification mentioned in chapter 2. The evolution is consistent with the imposed BCs. Temperatures are slowly changing at every height of the vessel. For instance, fixed the vertical coordinate at Y=5.85m, on that line the temperature sees a change of 0.0108°C/day. The situation is quite stable.

After the initial transient period shown in figure 5.3a, the magnitudes remain constant and the velocity conformation is stable. For this reason it is below reported only the situation in a single instant, in particular after 1'836'000s ($\approx$ 21 days) of simulation.

The **velocity magnitude** distribution is shown in figure 5.4.
The final order of magnitude which is computed by this simulation is $\mathcal{O}(10^{-5})$ m/s.

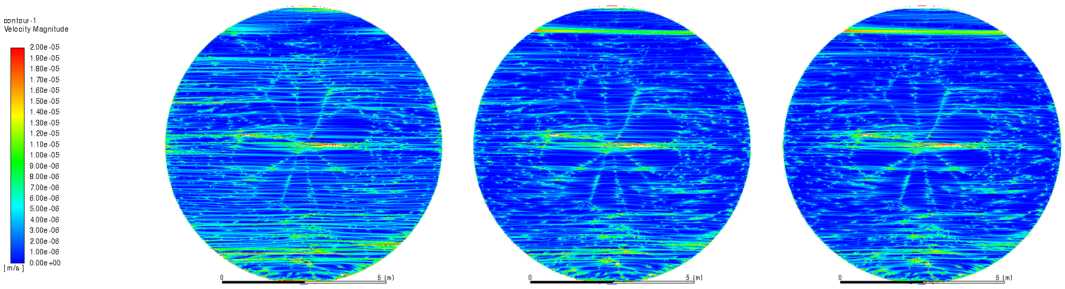

Figure 5.4. Velocity magnitude. From the left: base case, 1° and 2° interpolation.

It is possible to notice a higher velocity region in the bottom part of the IV with a clear motion stratification. In the central part, a peculiar leaf-shaped conformation is visible in the three cases. This is associated to numerical noise caused by a poor grid refinement. Finally, in the very bottom part, another nonphysical solution is present; this is again due to the grid.

The two interpolations generally reveal a lower velocity except for a thin layer close to the top. These are the expected effects generated by the small change in the BCs. The change is visible in the whole vessel; it is an evidence of how much sensitive the Borexino fluid-dynamics is.

More details on the effective inner motion are given by the **horizontal velocity**. The fluid shows a horizontal stratification in all the domain. This is absolutely

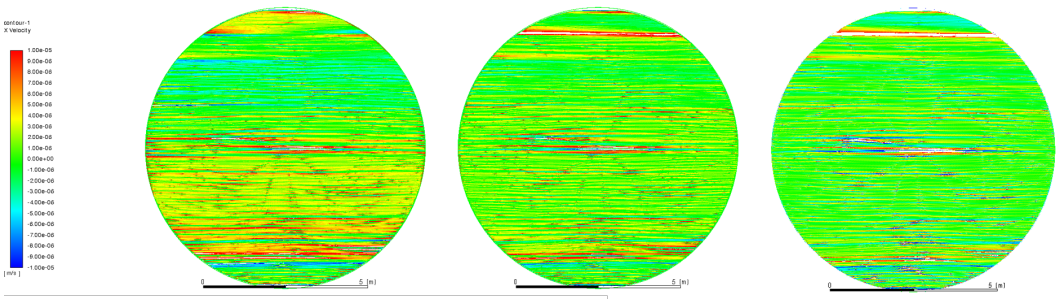

Figure 5.5. Horizontal velocities. From the left: base case, 1° and 2° interpolation.

confirming the results of the previous works. So, the model is telling us the vessel

has horizontal currents from left to right (red) and vice-versa (blue). The motion is more or less intense depending by the Y-vertical coordinate. In the middle and in the bottom part the movements seam to be directed towards the increasing X coordinate. The opposite in the higher part. Green colour means no, or very small, velocity. The effect of the numerical noise is again visible.

The 1° interpolation exhibits lower velocities, confirming the velocity magnitude trend. On the top it is still present a region of strong X-positive currents.

The 2° interpolation shows the lowest velocities for the middle/bottom part but even higher at the top (slightly out of the contour scale).
The general trend is well reproduced by all the three cases. The order of magnitude is consistent.

A final look at the **vertical velocities** should be given, see fig. 5.6.

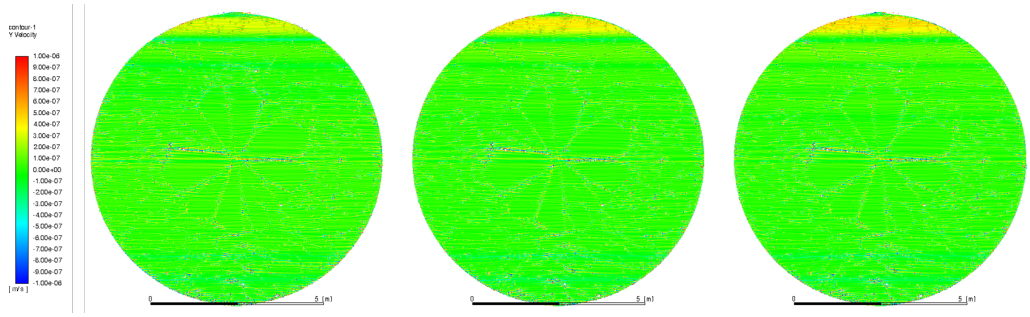

Figure 5.6. Vertical velocities. From the left: base case, 1° and 2° interpolation.

The Y-velocity is quite important since, in the past, a vertical change in ^{210}Po concentration has been noticed.
Here, the order of magnitude is $\mathcal{O}(10^{-6})$ m/s. This obviously suggests lower vertical currents. In the upper part a region of soft motion is identified, accentuated in the second interpolation case. In the rest of the domain, the velocity distribution appears to be caused by numerical noise; there are no clear structures.
More details on the vertical velocity accuracy will be given in the next section.

Another important feature is the **behaviour at the boundary**.

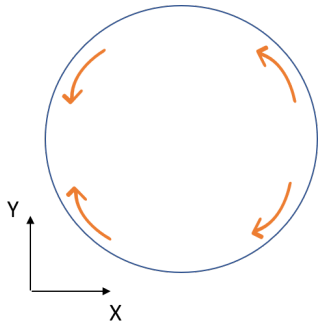

Figure 5.7. Schematic behaviour of the boundary fluid dynamics.

From an accurate scan of the velocity vector directions at the border, it has been possible to reconstruct the fluid behaviour. The scheme, which should be coupled

with figure 2.1, wants to summarise the main movements and it. The directions are simply decided by the temperature driven natural convection. Since temperature asymmetries are present at the border, hotter fluid tends to move upwards, while the colder regions move downwards. This is a perfectly physical tendency given by the small density variations.

5.2.2 Fine computational grid

The results from the more refined mesh are now presented. This grid counts 530k cells. This analysis has been carried out just for the base case and for the second interpolation. The first interpolation has been abandoned since it was giving less significant results. The presented results are taken at the same instant of the 270k cells grid.

Also in this case the velocities have been recorded for the first moments of the simulation. The monitoring points are the same of the previous analysis and are shown in figure 5.3b.

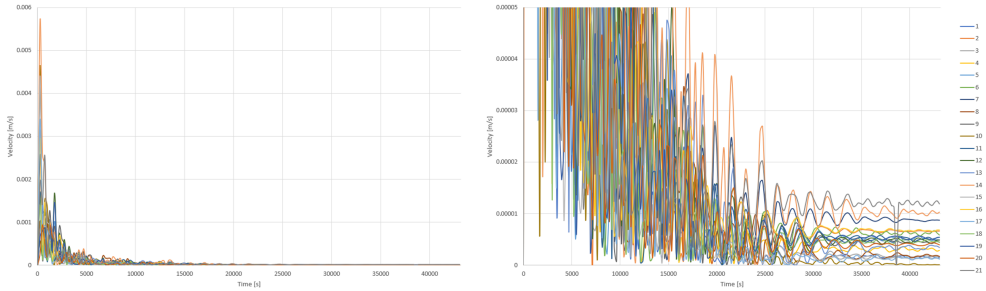

Figure 5.8. Initial velocity magnitude evolution – Base case.

Again, the velocities perceive a fast increase at the very early moments and afterwards they stabilise. In the right image, it is possible to notice how the oscillations continuously reduce until reaching a constant and very small amplitude around 35'000s. After this time the situation can be considered stable.

An important difference, compared to the 270k cells case, is that the numerical noise seems to be disappeared. This happened thanks to the grid refinement.

The order of magnitude for the **velocity magnitude** in unchanged. Always a bottom part characterised by higher velocities is denoted. Generally, it appears that the velocities are more equally distributed in the vessel. The interpolation again brings lower velocities and maintains peculiarities in the top part.

Looking at the ***X*-velocity**, the horizontal currents are very well confirmed. The stratification is even more accentuated and the distribution presents flows both to the right and to the left.

The interpolation softens this attitude but does not deny it. Two regions, at the top and at the bottom, show high velocities towards the right direction. At the very top instead, the tendency is the opposite.

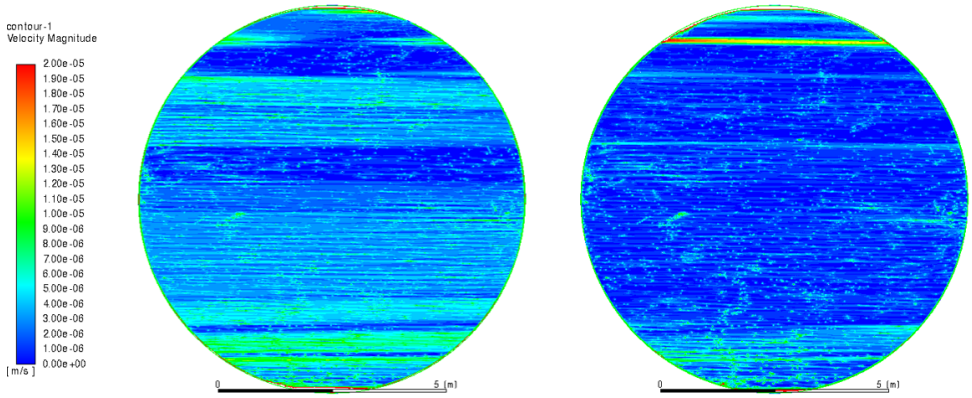

Figure 5.9. Velocity magnitude. From the left: base case and 2° interpolation.

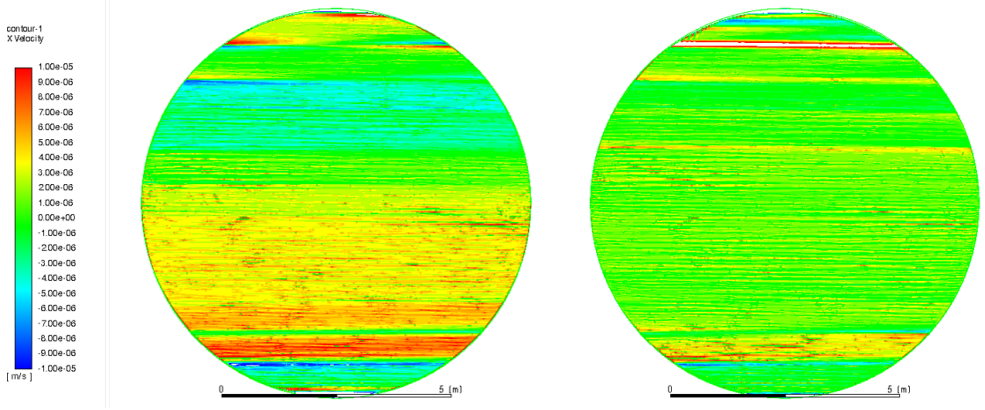

Figure 5.10. Horizontal velocity. From the left: base case and 2° interpolation.

The **vertical velocities** are quite similar to the 270k cells case; the topmost part presents positive magnitudes. Other horizontal bands of lower magnitude ($3.5 \cdot 10^{-7}$m/s) can be appreciated always close to the top. In the rest of the domain no clear structures are denoted. A study of the magnitude distribution has been carried out thank to the histograms option of FLUENT; results are shown in figure 5.12.
The higher percentage of the velocities is close to zero. The main peak is centred in $0.85 \cdot 10^{-7}$m/s and another small one is visible to the right. This is probably not enough to distinguish a physical distribution from the numerical noise. Anyway, it is the most accurate result concerning the vertical velocities.

The **behaviour at the boundary** is exactly the same compared to the 270k cells case. The temperature asymmetries are unchanged and thus, also the various fluid movements maintained the same shape.

To sum up and give an overall view of the 2D fluid-dynamical results, the table below is presented.
It is possible to notice how the average cell size is decreasing. The vertical and horizontal velocities are taken from an accurate study of the presented contours. The reported values are the *maximum magnitudes* detected.
The velocity at the boundary is given by the analysis of the vectors. Ii is important

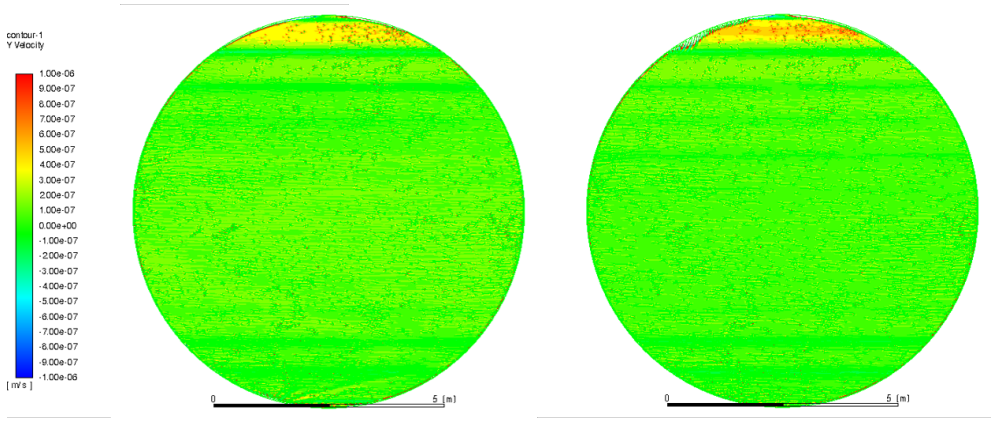

Figure 5.11. Vertical velocity. From the left: base case and 2° interpolation.

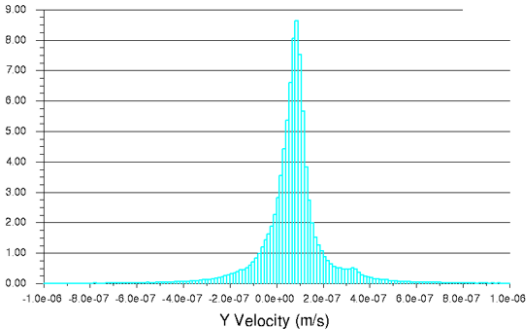

Figure 5.12. Vertical velocity distribution.

N° cells	Surface [m^2]	Average elem. surface [m^2]	Average cell size [m]	Velocity at the boundary [m/s]	Vertical vel. [m/s]	Horizontal vel. [m/s]
270k	$5.67{\cdot}10^{1}$	$2.09{\cdot}10^{-4}$	0.0144684	$3.00{\cdot}10^{-4}$	$1.00{\cdot}10^{-6}$	$2.00{\cdot}10^{-5}$
530k	$5.67{\cdot}10^{1}$	$1.07{\cdot}10^{-4}$	0.0103432	$9.00{\cdot}10^{-4}$	$1.00{\cdot}10^{-6}$	$1.10{\cdot}10^{-5}$

Table 5.1. Geometry and fluid-dynamics results of the 2D simulations.

to underline that in the second case the maximum velocities are increasing. This is due to the different mesh structure (see fig.4.1b) which is able to better reproduce the fluid behaviour close to the border.

5.3 Overall comparison of the 2D Polonium concentration

Finally, the ^{210}Po distribution in the Fiducial Volume is computed. The different velocities taken from the various cases are inserted in COMSOL and the Polonium predictions are compared to the experimental measured values. The concentration is reported in *count per day every* 100t of fluid.

The base cases and the second interpolation results are plotted. The present values

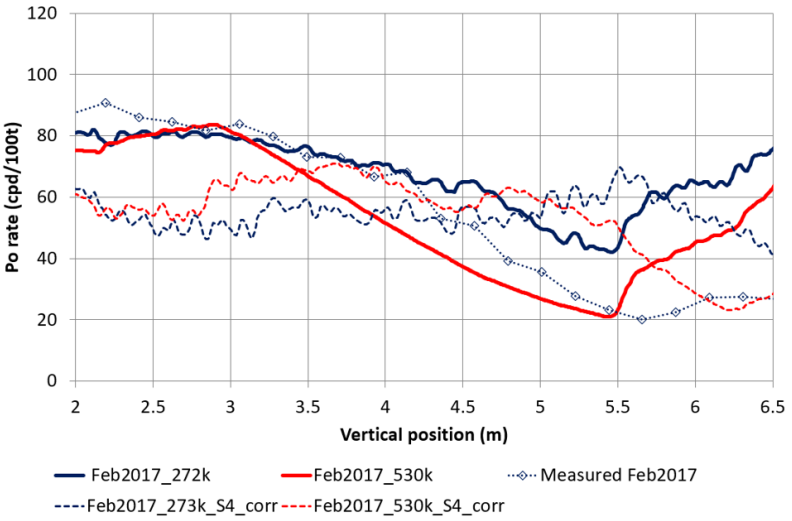

Figure 5.13. Polonium distribution over the vertical coordinate of the Fiducial Volume.

are an average over the horizontal position.
The measured values for the period show a higher and quite constant trend in the bottom part of the vessel. Going up throught the vessel, the concentration is decreasing until a minimum is reached at a position of ≈5.6m.
The calculated values, mainly determined by the convective currents, reveal some discrepancies. The distributions of the base cases (blue and red lines) softly underestimate the measured data in the lower part of the volume and overestimate it in the topmost part. Both present a minimum at a height of 5.5m which qualitatively approaches the experimental trend. The 530k cells prediction is also in agreement from a quantitative point of view.
The results of the interpolation instead (dash lines) are quite far from the real data. The bottom underestimation is evident. 270k cells presents no minimum even if the concentration is going down at the higher coordinates. The 530k reaches a minimum at 6.2m which is quantitatively consistent. These strong differences from the base cases are generated by the imprecise temperature BCs of the *WR* model and the high sensitivity of the system. It has to be reminded that only three out of seven imposed external temperatures are related to the height of the IV, and one of it, the s4, is even denoted by an imprecise position.

These results are generally satisfying from a qualitative point of view. The ^{210}Po concentration trend is quite well reproduced by the base cases and similar for the 530k cells with interpolation. The refined mesh gives more precise results concerning the fluid-dynamics, but the temperatures at the border are still not fully reliable.

Chapter 6

Results of the 3D cases

The characterisation of the 3D model through the study of the results coming from different meshes constitutes the majority of the present work.
This analysis presents different targets. First of all, the comparison between the bi-dimensional and tri-dimensional models. Moreover, several sensitivity analysis regarding the average cells size and the time step are computed. Finally, considerations concerning the reliability of the whole model are inserted.
The length of the simulations really depends by the employed mesh and the computational resources. Considering that for the 3D cases only the IV simulation is run, the total time varies from 2 weeks to more than 1 month. For this reason, only the faster simulation has been effectively run until the end. In the other cases, a trade off is reached between the obtained results and the spent time.
In general, the evaluation deals with the flow field study and the velocity evolution given by the several considered computational grids. The boundary conditions are referred to the *WR base case* for all the run simulations. Thus, the results will be compared to the related 2D cases.

In order to simplify the reading, a general scheme of the 3D analysis is shown in figure 6.1.
First of all, the evolution of the results coming from the three coarser meshes is presented. Additionally to this study, two tests are thought to better understand the arisen differences among the rotational spin of the internal bulk. Secondly, a time-step sensitivity analysis is computed in order to evaluate the model convergence and precision. Moreover, the effects of a different BL structure is investigated on the very fine mesh of 10M of cells, obtaining a grid with 10.2M of cells.
After these passages, a final and summarising simulation has been run with the scope of obtaining the most precise results. The velocity field of this last model is then employed for the computation of the ^{210}Po concentration. All the simulations are computed in FLUENT except for the mass transfer model, orange in the scheme, for which COMSOL Multyphisics is used.

A full presentation of the 3D geometry of the computational grids is already given in section 4.1.2. From now on, the various meshes will be associated to their number of cells.

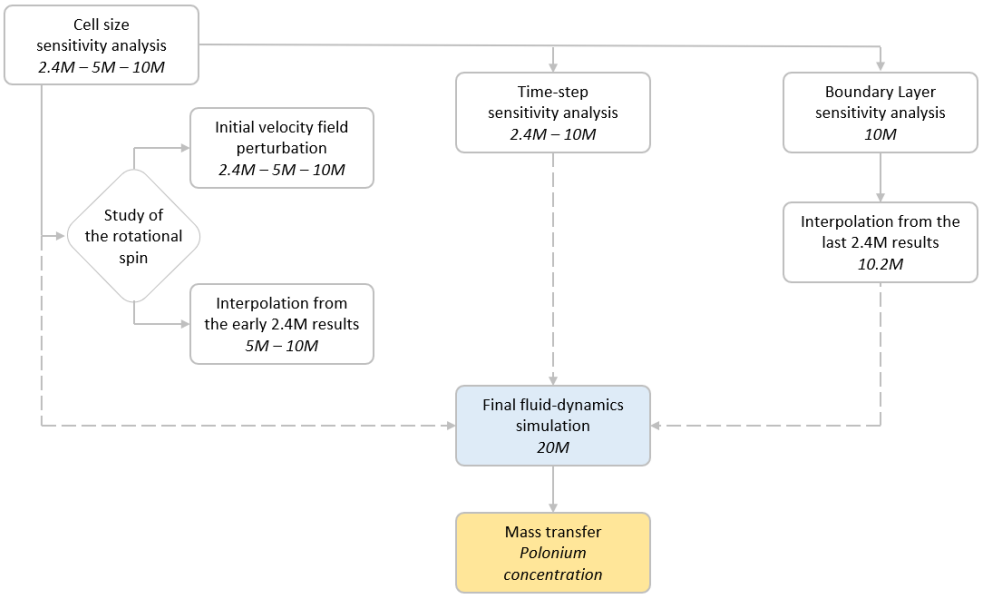

Figure 6.1. Complete scheme of the 3D analysis.

6.1 Cell size sensitivity analysis

The computational grids considered in this analysis are the first employed in the 3D study. The starting point is a coarse mesh, with 2.4M cells, which anyway permits to obtain a general idea of the fluid-dynamics. Increasing the number of cells we arrive to a finer mesh of 10M cells. The early approach to the tri-dimensional problem was also characterised by the understanding of the needed time and computational efforts. The simulations were quite slow, for this reason not all of them have been computed to the end. None of the three simulations presented in this section reached a clear and complete convergence. The table below is thought to give a general overview of the length and of the time-step of the three simulations.

N° of cells	Time-step [s]	Computed time [s]
2.4M	9	850000
5M	4.5	432000
10M	4.5	777600

Table 6.1. Time characteristics of the basic simulations.

The comparison has been carried out on the last available data for all the simulations, at **432'000s**. It will be clear that, at that time, the velocity evolution was still in progress. Anyway several considerations could be already taken.
The time-step is decreasing with the target of maintaining an appropriate low Courant number with the change of the cells size.

To visualised the results, the vertical plane (ZX) which cut in two the sphere is created. Other horizontal planes (XY) are afterwards generated to give a complete view of the system and to study the evolution at different heights. It can be useful to remind that the BCs are symmetrical compared to the ZX plane.

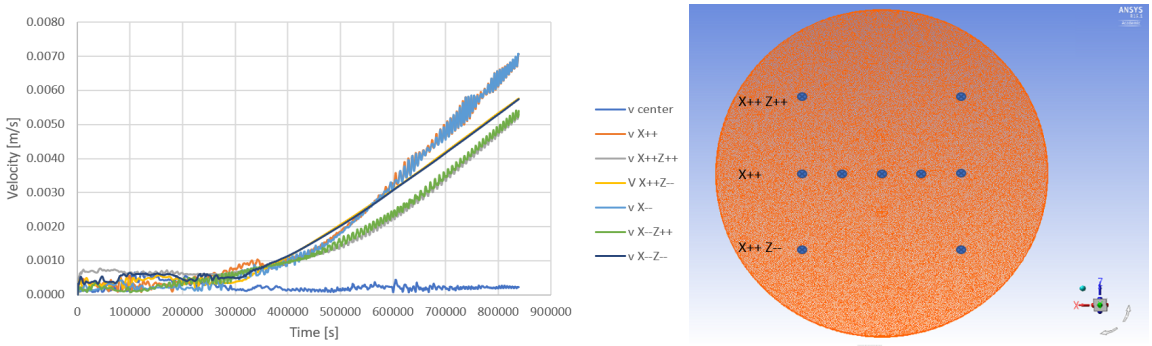

(a) Velocity magnitude evolution for the 2.4M of cells. (b) Monitoring points.

Figure 6.2

The 2.4M velocity evolution is monitored at different points on the mentioned vertical plane.

After a long initial stationary period, the velocities start to rise, maintaining partially an oscillatory behaviour. It is interesting to see how the evolution begins around 350k seconds; in the 2D cases, only few thousands of seconds were needed to reach convergence to a final stable solution. From this image it is not possible to understand when the increase will stop; in the next section are presented the results of a simulation which finally stabilised. For the 5M and 10M cases the evolution is similar but even slower.

The velocity of the center remains close to zero. This can be easier understood from the following pictures. The **velocity magnitude** is here reported.

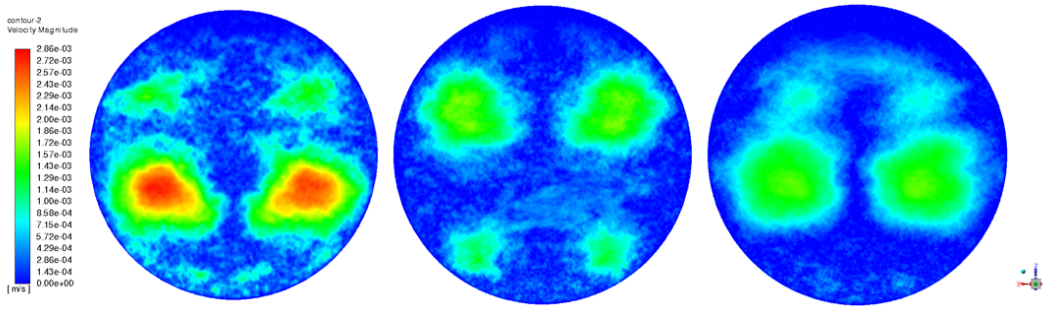

Figure 6.3. Velocity magnitude – ZX plane. From the left: 2.4M, 5M and 10M.

The most important feature to be underlined is that the order of magnitude of the velocities is $\mathcal{O}(10^{-3})$ m/s. It is quite far from the bi-dimensional case.
Furthermore, the magnitude is higher for a lower number of cells. There are two possible explanations for this behaviour. First, the evolution is slower increasing the number of cells. Second, that increasing the number of cells, and so the resolution, the final velocities at convergence will be lower. This second option makes more sense; in fact, *with a more refined mesh the solution is tending towards similarity to the 2D*. The 20M case is going to confirm it.
The three cases are also evolving differently. While the 2.4M and 10M are faster in the bottom part, the remaining presents the peaks in a higher position.

The physical behaviour is clarified by the **Y velocity**. This is the component entering and exiting from the visualised plane.

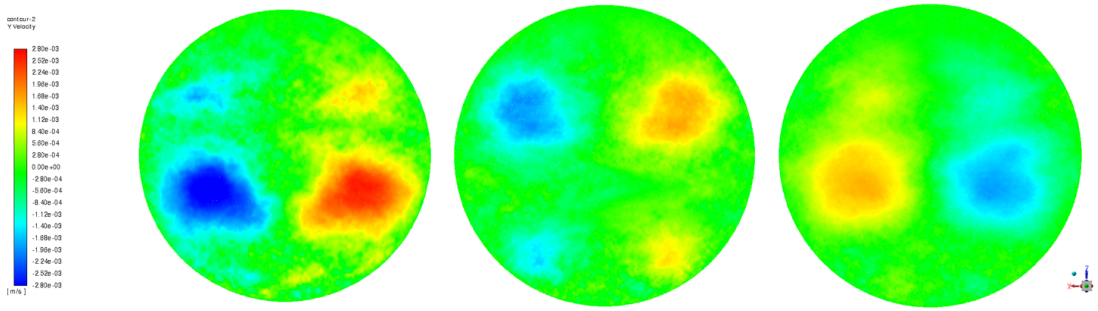

Figure 6.4. Y velocity – ZX plane. From the left: 2.4M, 5M and 10M.

These figures reveal that currents perpendicular to the plane are present. It is also possible to understand that this currents are rotating around the vertical central axis; so, some vortex structures are generated. *The horizontal currents seen in the bi-dimensional case and in previous studies are confirmed. The rotational behaviour is instead a new feature which characterises the 3D results.*

Another paramount fact is that the 10M case is spinning in the opposite direction compared to the others. As said before, horizontal planes are exploited. In the next image it is possible to better appreciate the rotational directions thanks to the vectors visualisation. The reported cut is 1m under the middle plane.

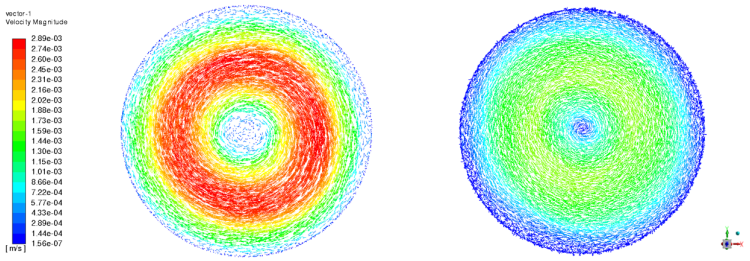

Figure 6.5. Velocity vectors coloured by V magnitude – XY plane, Z=5.85m.
From the left: 2.4M and 10M.

On the left, with a clockwise spin direction, the 2.4M case. On the right, counter-clockwise, 10M of cells. More investigation about this question is conducted in the next section.

To have a complete idea of the velocity field, the **vertical velocities** are also given.
Once again, the higher number of cells produces lower velocities. No clear structures are present here. The distribution seems to have a numerical noise nature. The order of magnitude, as for the 2D cases, is one order lower than the other velocities, $\mathcal{O}(10^{-4})$ m/s.

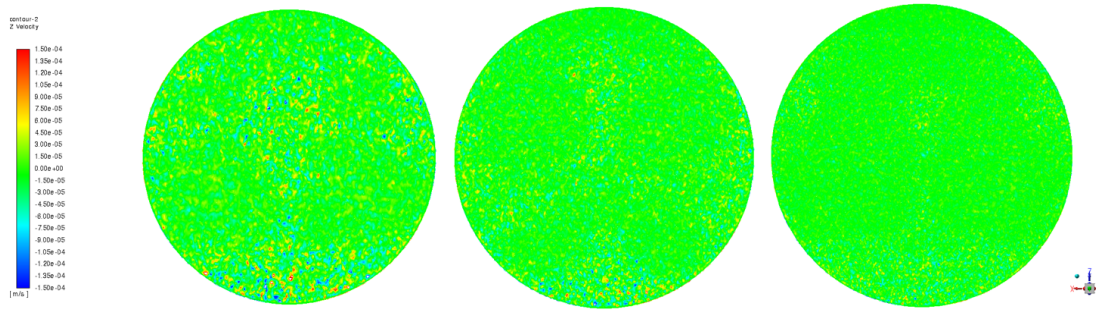

Figure 6.6. Z velocity – ZX plane. From the left: 2.4M, 5M and 10M.

The bottom part reveals more movements in all the cases. From an accurate look to more updated data, it is possible to infer that the vertical velocities show up in regions where the other velocity components are weaker. This is the case of the bottom region and, most relevant, the area around to the vertical axis. This is still not so clear from figure 6.6 because the results are in strong evolution.
A more detailed quantitative analysis on the vertical velocities is present in section 6.4.

To better investigate the **velocity and temperature profiles** and their evolution in time, data have been extracted from horizontal lines at different heights in the ZX plane.

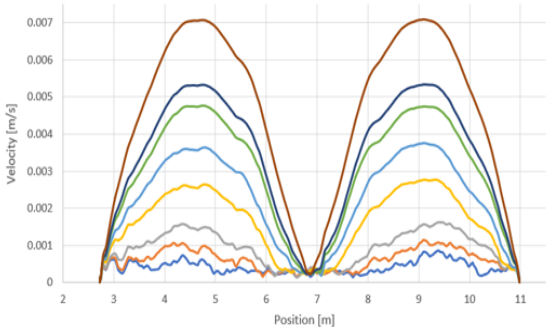

(a) 2.4 million cells.

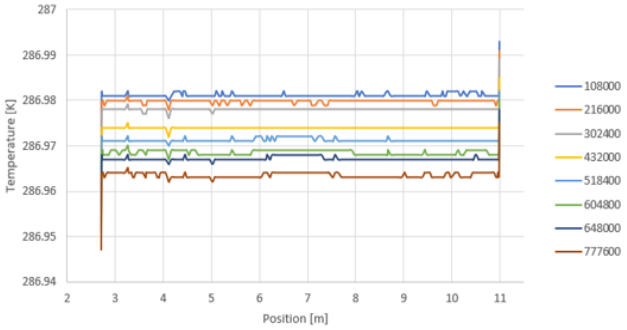

(b) 2.4 million cells.

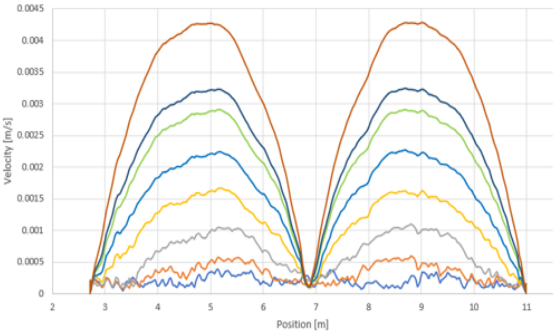

(c) 10 million cells.

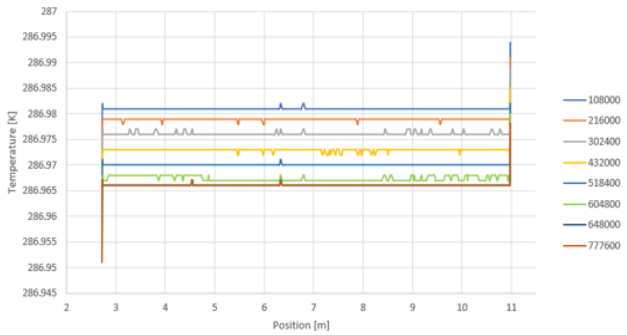

(d) 10 million cells.

Figure 6.7. Velocity magnitude and temperature evolution at Z=5.85m.

These lines are located where a higher velocity magnitude is noticed. In figure 6.7,

the profiles 1m under the middle plane are reported. Temperature trend on different lines is very similar; the velocity one depends more by the structures evolution but, soon or later, the same shape is re-proposed.

Considering the velocities first, it is clear that around 300'000s the velocity magnitude starts to evolve in both cases. The increase maintains the linear behaviour seen in fig.6.2a. It can be noticed, from the scale, that there is a constant proportion of ≈1.65 between the two cases. This value is very similar to the proportion between the average cells size of the 2.4M and 10M (see table 6.2).
The BCs are respected at the borders, indeed the fluid is motionless. The profile is symmetrical compared to the central axis, where the magnitude is close to zero.

The temperatures are in both cases decreasing with a rate of 0.00288°C/day; the evolution is slower than the 2D case. The isotherms stratification is again confirmed. The two peaks at the boundaries are given by the BCs.
There is not a well denoted relationship between the velocity and temperature distributions.

The **behaviour at the boundary** perfectly matches the bi-dimensional situation in the ZX plane. The motion follows the physical tendency driven by the natural convection. For the ZY plane the behaviour is symmetrical, this is expected given symmetrical BCs as well.

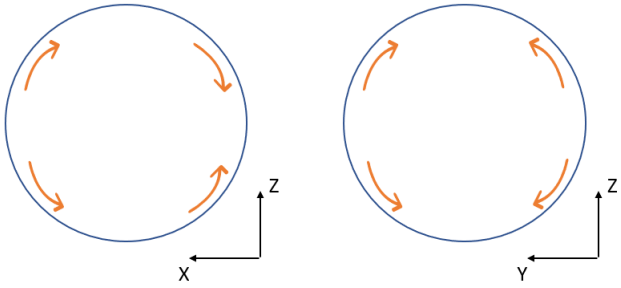

Figure 6.8. Schematic behaviour of the boundary fluid dynamics – ZX and ZY planes.

All these movements tend to fade away with time, when the whole velocity field is developed.
The values of the maximum velocity intensity are given in the table below. Refining the mesh, the velocities are increasing. This is because the grid has a better computational resolution. The values are approaching the 2D cases; this means that the choice of the structured layers of cells at the border is positive.

The average cell size is reported in column n°3. This is a good indicator which can tell us how close we are to a faithful reproduction of the 2D model. It is clear that the 3D, at the moment, is quite far from it; for the 10M, the cell size is at least three times bigger than the best 2D case.
The vertical velocities are one order of magnitude higher compared to the 2D case. Anyway, it can be said that the maximum values are decreasing and very slowly approaching the bi-dimensional results.
Horizontal velocities are taken from contours in the ZX plane. This is done in order to compare them to the 2D. Also for these values, the intensity is one order of magnitude

N° cells	Surf.–Vol. [m^2 – m^3]	Average cell size [m]	Velocity at the boundary [m/s]	Vertical vel. [m/s]	Horizontal vel. [m/s]
270k	$5.67{\cdot}10^{1}$	0.0144684	$3.00{\cdot}10^{-4}$	$1.00{\cdot}10^{-6}$	$2.00{\cdot}10^{-5}$
530k	$5.67{\cdot}10^{1}$	0.0103432	$9.00{\cdot}10^{-4}$	$1.00{\cdot}10^{-6}$	$1.10{\cdot}10^{-5}$
2.4M	$3.22{\cdot}10^{2}$	0.0511671	$5.00{\cdot}10^{-4}$	$6.00{\cdot}10^{-5}$	$1.50{\cdot}10^{-4}$
5M	$3.22{\cdot}10^{2}$	0.0400625	$6.00{\cdot}10^{-4}$	$5.00{\cdot}10^{-5}$	$5.00{\cdot}10^{-4}$
10M	$3.22{\cdot}10^{2}$	0.0317976	$7.00{\cdot}10^{-4}$	$3.00{\cdot}10^{-5}$	$1.70{\cdot}10^{-4}$

Table 6.2. Geometry and fluid-dynamics results of the simulations.

higher. The trend evolution is not so clear as for the vertical velocities.

To sum up, in general it can be said that the three models generate qualitatively similar results. A spin around the vertical axis is denoted and the same behaviour at the boundary is detected. Finally, the vertical velocity seems to be related to the numerical noise.
The big differences are concerning the shape of the velocity evolution. For the 5M cells the velocity is arising faster in the topmost part of the vessel, while for the other cases is the opposite. Another relevant problem is the reverse spin of rotation of the 10M cells mesh. Considering that the imposed BCs are the same, it has to be understood to what the nature of these differences is related to. Two tests, thought to investigate this issues, are presented in the next subsections.

6.1.1 Test 1: Initial velocity perturbation

The first attempt to dig in the nature of the differences shown by the 3D models is related to the initial velocity map. The idea is to understand if a perturbation in the initial velocity can bring to a different solution or can even affect the fluid spin of rotation. This could tell us if the differences are due to an initial setup choice or are more linked to the mesh.

In the cases presented before, the velocity map is initialised to a very low magnitude. This choice is made in order to let the evolution start spontaneously. The velocities, in all the grid points, were set: $V_x = V_y = 1 \cdot 10^{-10}$m/s and $V_z = 0$ m/s.
In the new perturbed cases, the velocities are instead set: $V_x = V_y = 1 \cdot 10^{-2}$m/s. This values are chosen higher than the ones reached by the previous solutions. This way, if the models are reliable, they should converge to the same results. This is also giving an initial well-determined velocity direction which could bring to a change in the spin direction.

The test is computed for all the three cases. The simulated time is starting from the beginning and the cases proceed until the solutions are comparable with the previous ones, around 120'000s. Since a time-step of 9s is giving convergence also for the 5M and 10M meshes, this value is chosen in order to speed up the analysis; clearly, the results have a precision slightly worst compared to the base cases, but

they are giving both a qualitatively and a quantitatively acceptable feedback.

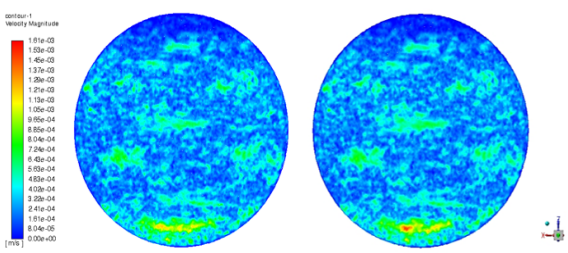

(a) Velocity magnitude – ZX plane
From left: base and perturbed case.

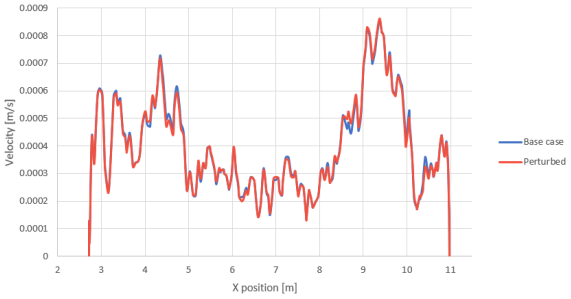

(b) Velocity magnitude profiles at Z=5.85m.

Figure 6.9. 2.4M of cells – 129'000s

In figure 6.9. from the left we can see how the perturbed **2.4M** case is equally evolving to the base case. The velocity magnitude distribution on the ZX plane is perfectly reproduced. The same high velocity areas are denoted. The magnitude is slightly higher in the bottom part.
The plot, instead, helps to visualise the effective velocity distribution on a horizontal line. The two cases are overlapped except for some small peaks variations. These negligible differences are probably due to the high initial velocity, the solution is still arranging. This is also true for the other lines at different heights.

The same situation is found for the 5M and 10M cases. Here is reported the **10M** case in order to have a direct comparison.

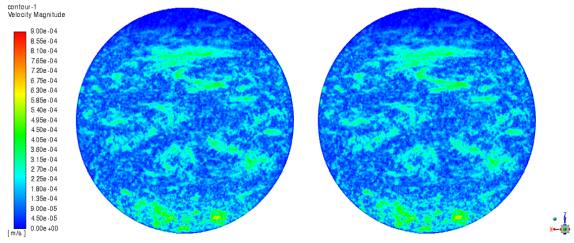

(a) Velocity magnitude – ZX plane
From left: base and perturbed case.

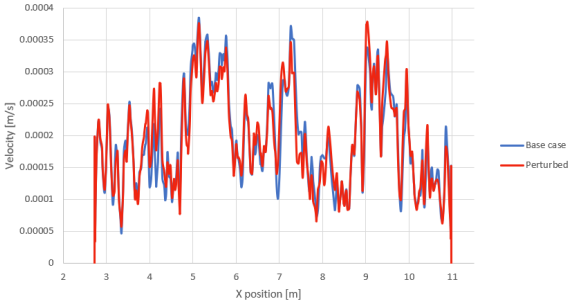

(b) Velocity magnitude profiles at Z=5.85m.

Figure 6.10. 10M of cells – 129'000s

The same considerations of the previous case are valid. In the plot, the more visible differences are also due to the time-step change; the larger Δt (from 4.5s to 9s) is probably subtracting precision to the solution. Giving a look to the Y velocities, can be inferred that the spin of rotation is not altered.
This analysis can bring to the conclusion that the actual velocity evolution and the spin rotation direction are not dependent on the starting velocity map.

The study is also giving credit to the reliability of the solution, since the initial high velocities tend to decrease and converge to the same solution of the base case.

Anyway, the question about the different spin of rotation still remains. It seems that the solution is strongly affected by the mesh itself. Moreover, at the moment it is not clear how far we are from the effective final velocity distribution; it can also be true that, at the end, the 2.4M and 10M will give exactly the same solution but with an opposite rotational direction. In this case the effective spin direction could lose part of its relevance.

6.1.2 Test 2: Interpolation from the coarse mesh solution

The second test done to understand the differences between the three meshes solutions is presented. The focus is now fixed on the spin of rotation. An intermediate solution of the 2.4M cells case is interpolated and inserted in the other two cases. So, the 5M and 10M cells grids are here exploited to continue the evolution started with the 2.4M cells. This way, it will be possible to see if the evolution is really different and, for the 10M, if the spin will slow down and change direction.

It is chosen a starting point from which the solution is interpolated, exactly 518'400s. The data can be after inserted in the bigger meshes.
The interpolated solution is not containing the time-step information. So, Fluent launched the new simulations from a random time-step. In this case the imposed BCs are different. Since the idea of the test is to compare the evolution of the solutions, if the BCs are similar the comparison is still valid.
The temporal information of the two simulations are present in the table below.

N° of cells	Time-step [s]	Starting point [s]
5M	9	49500
10M	9	2084

Table 6.3. Temporal information of the test 2.

Thus, the first step is to check if the BCs, in the interested period, can be considered similar to the one imposed to the 2.4M case. The fact that the starting point is changing implies that the comparison has to be made visualising the $\Delta time$ passed from the beginning. With this reference, it will be clear how fast is the velocity growth.
It can be noticed that, as for the previous test, the choice of the time-step is 9s for both cases. This is done again to decrease the computational cost and time.

The simulations are run for a length of 180'000s. The values of the boundary imposed temperatures are checked in six different positions, see fig. 6.11. The points are chosen at different heights and on both north and south sides. The temperature profiles are reported in the next plots.

The magnitudes are obviously different between north and south. The most important feature which can be underlined is that the temperature difference between the various simulations is always < 0.02°C. It is true for all the monitoring points. This can be considered a reasonably small ΔT. So, being in a moment of strong evolution for the velocity magnitude, it can be said that the development of the new solutions

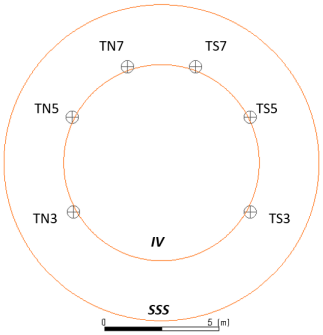

Figure 6.11. Position of the BCs check points for the comparison.

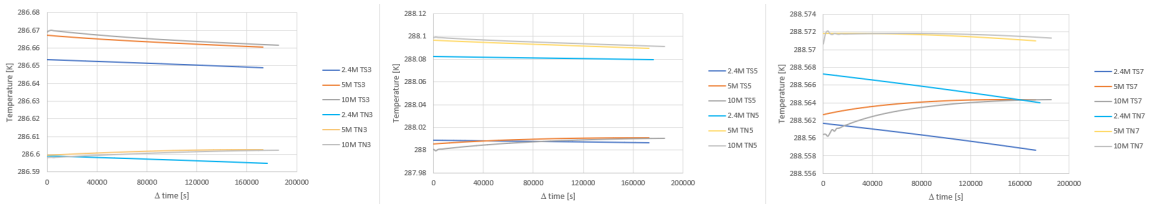

Figure 6.12. BCs at the points N°3, N°5 and N°7.

are comparable to the old ones.

To visualise the evolution of the 2.4M cells and the two interpolated cases the Y-velocity in the ZX plane has been chosen. These contours can well emphasise either the differences in the vertical evolution and in the velocity magnitude.
The next figure wants to summarise the evolution of the solutions in all the 3 meshes. The base case is on top and the two interpolations downwards. The scale is unchanged in all the contours.

It can be seen how, in all cases, the velocities are growing up towards the topmost part of the IV. This means that the fluid rotation around the vertical axis is developing at every height. It is happening in all the simulations, denoting once again the reliability of the solution.
In the 5M cells case the behaviour is very similar to the 2.4M. From the last profile it is clear that the velocity is evolving more smoothly, the conformation of these big regions of high magnitude is well denoted.
The 10M solution brings to an interesting consideration. Apparently, the trend is quite the same compared to the other interpolation. The velocity conformation is even more precise and smooth. It is also true that the Y-velocity intensity is less strong. This is due to the higher number of cells which guarantees a higher resolution (see also fig.6.14). The paramount fact is that no decrease of the velocities and change in rotational spin of direction is shown. Actually, the velocities continue to increase. So, it can be inferred that the effective direction of rotation is not driven by a physical solution but it is part of a stochastic process. Of course, the number and the distribution of the computational cells play a fundamental role in this process. The initial moments of the simulations are crucial for the whole development; every difference in the mesh conformation could bring to a non-identical solution and thus, opposite rotational spin.

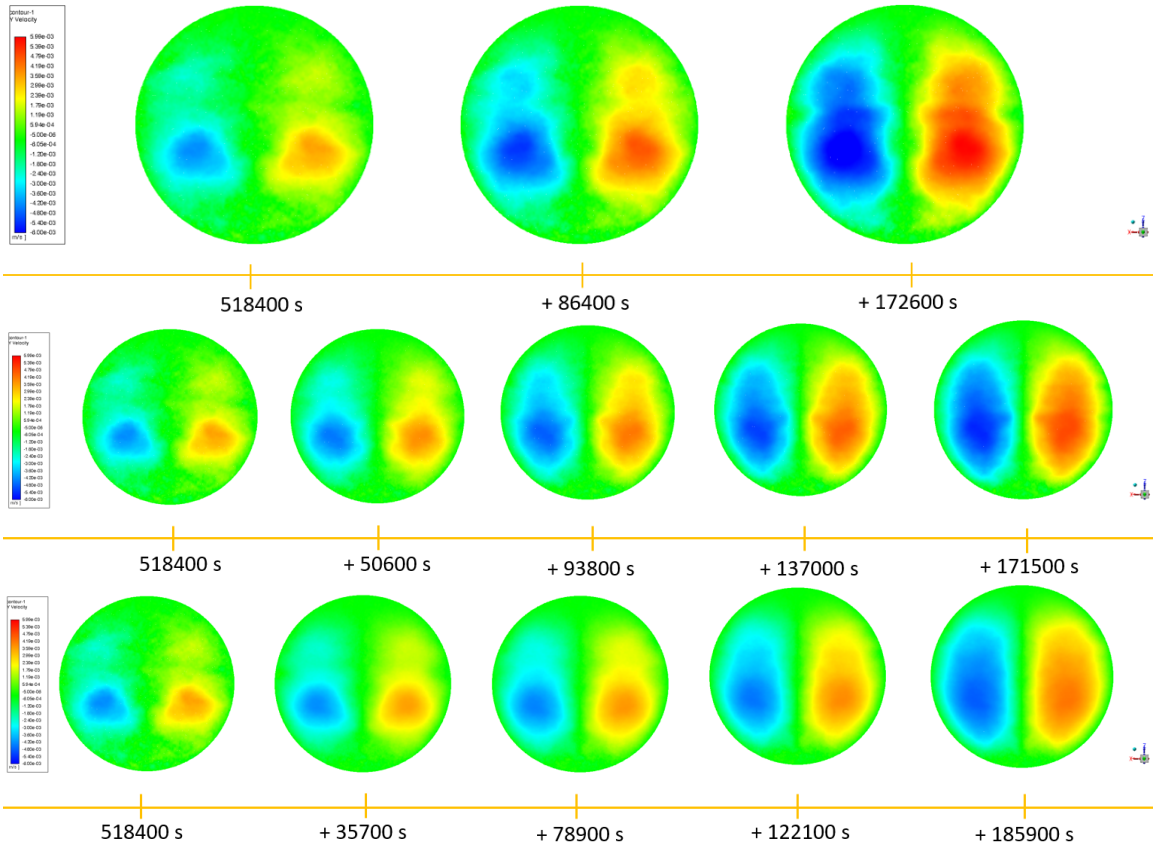

Figure 6.13. Interpolation velocity magnitude evolution. From the top: 2.4M, 5M and 10M.

The purpose of this last plot is to give the idea of the three velocity trends during the simulations. The starting common velocity is the one reached at the moment of the interpolation, 518'400s. These are the values recorded in proximity of the higher magnitude points in the ZX plane; so, they are punctual.

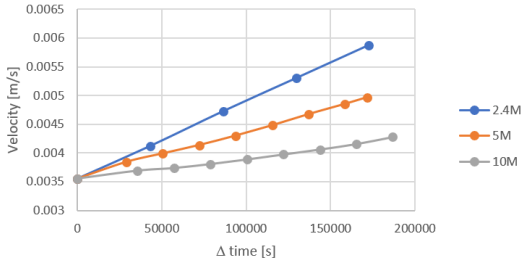

Figure 6.14. Punctual velocity trend – $X = 4.65m$ / $Z = 5.85m$

The behaviour has been checked in several positions and it is consistent.
It is like the heavier mesh has a slower increase. Again, the explanation is that its better resolution is able to approach a more physical solution. As seen in the 2D cases, this solution reveals lower velocities. Thus, the 10M cells case is simply approaching different final magnitudes compared to the 2.4M cells.

The question concerning how long a simulation should run until a stable solution is reached is still open. Part of the next section is devoted to this problem.

6.2 Time-step sensitivity analysis

At the beginning of the simulations a sensitivity analysis on the time-step has been carried out in order to understand and visualise if the adopted time-step was accurate enough. This has been done for the meshes with 2.4M and 10M of cells.
The original time-step is halved; this way, it is possible to compare the velocity profiles. In order to visualise the outputs, the profiles are extracted on horizontal lines at various vertical positions. In the case of different results, the new time-step is chosen to continue the simulations.

For the **10M cells computational grid** the time-step passed from 4.5s to 2.25s. Since the simulation was slow, the comparison is computed in a short period.

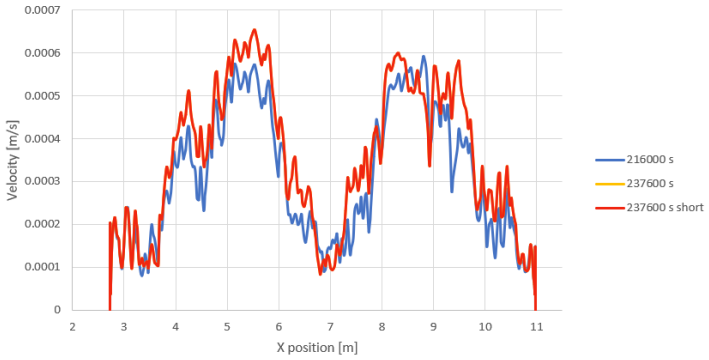

Figure 6.15. Velocity magnitude evolution with different time-steps at Z=5.85m – 10M cells.

Starting from 216'000s, the new simulation is run for 6900 time-steps. In this period the magnitude is increasing, of course. Most important, can be noticed that the new solution (red) and the old one (orange) are perfectly overlapped. At other eights the trend is confirmed. This can prove that a $\Delta t = 4.5$s is enough to gain a good accuracy for this case. Thus, the initial value is kept until the simulation in stopped.

The **2.4M cells mesh** brought to different considerations.

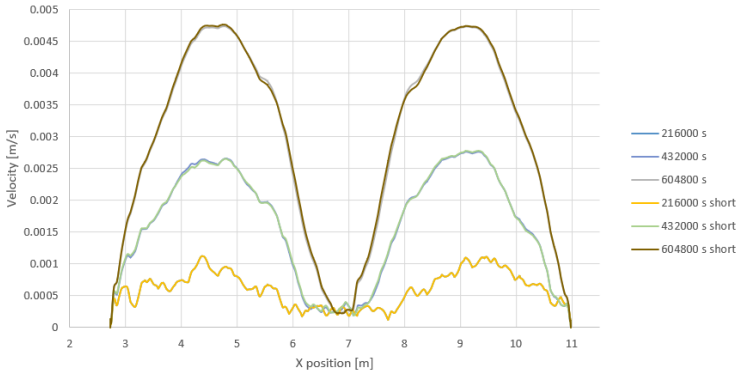

Figure 6.16. Velocity magnitude evolution with different time-steps at Z=5.85m – 2.4M cells

The time-step was here changed from 9s to 4.5s.
The solution is very similar but not the same. The profiles show small deviations in several positions. The comparison is done for different moments quite far in time.
In order to reach a more precise solution, the new $\Delta t = 4.5$s is employed. The old simulation is stopped, see table 6.1, and the new one is maintained. Thus, the simulation employing the coarse mesh with a $\Delta t = 4.5$s is the only one which arrived to completion. This permitted to appreciate the whole velocity evolution until convergence.

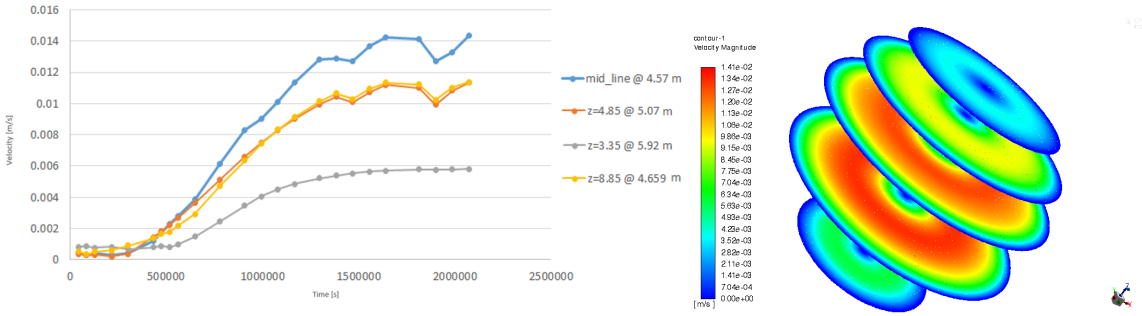

(a) Velocity magnitude evolution at different heights – 2.4M cells / $\Delta t = 4.5$s.

(b) Final vel. magnitude

Figure 6.17

This graph is obtained through the extraction of the velocity values in precise spots at different heights. The evolution is punctual and the X-coordinate is specified in the legend. A sort of plateau is reached around 1'400'000s. At that point the solution is quite stable, except for some oscillations. The final order of magnitude for the velocity is $\mathcal{O}(10^{-2})$ m/s. From figure 6.17b it can be seen how the spin around the vertical axis is now present at every height. The velocity is more homogeneously distributed. On the top and on the bottom the magnitude is shading.
This figure can give the idea of the slowness of the model evolution.

Since a mature solution is now available, this is exploited as a starting point for the heavier simulations, 10.2M and 20M of cells. This way, the velocity field is already developed and a new stable solution for the two models can be faster reached.

6.3 Boundary layer sensitivity analysis on the very fine mesh

Starting from the very fine mesh with 10 millions of elements, the 10.2M cells grid is designed to give a direct idea of the impact of the BL structure. The basic 10M grid already has a 6-layers of cells structure on the boundary; this is now changed. The other geometrical parameters are maintained constant, thus, being the sum of the layers thinner, the number of cells is slightly higher. Since for the bi-dimensional 530k case the employment of the structure with 7 layer of cells totally 2cm thick brought to satisfying results, the same pattern is re-proposed in 3D, see fig. 4.2b.

As introduced in the previous section, the simulation is characterised by a new initial approach. The last 2.4M solution is interpolated and inserted in the current case. In this way the velocities are already set to a fully evolved solution. A sort of transitory is then expected in order to finally reach the stable 10.2M configuration. The hope was that the evolution could advance faster than the previous cases.

The velocity magnitudes are extracted during the simulation in precise spots, the same of the 2.4M case (fig. 6.2b). The results are show in the next image.

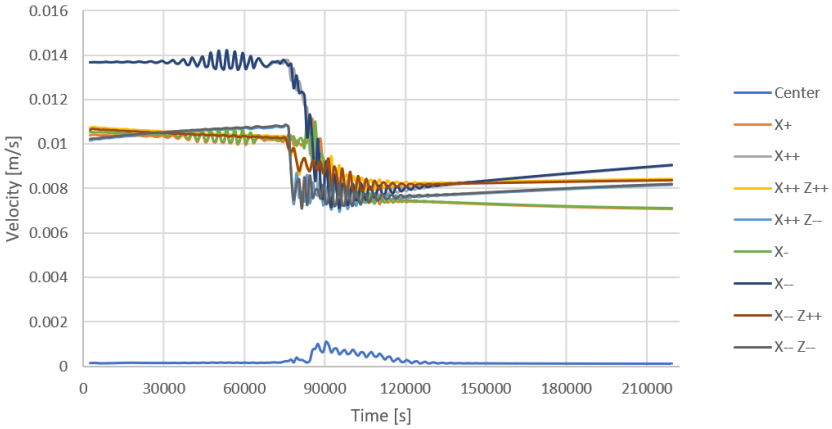

Figure 6.18. Velocity magnitude evolution.

After a constant initial trend, a first oscillatory behaviour is present around 60'000s. Immediately afterwards, the velocities start to fall and a strong perturbation is experienced by all the monitoring points; this can tell us that probably all the volume passed through a rearrangement of the velocity field. The light-blue line, checking the velocity of the central point, can well describe the perturbation history. It is clear that around 120'000s a new stability is achieved. The final order of magnitude is decreased.
In the right part of the plot can be seen how the majority of the monitored velocities are tending to a constant value around 0.008m/s. The simulation is then stopped because no other extraordinary evolution is foreseen.

As expected, an intermediate transitory passage is shown. This happens quite soon in the simulation and gives validity to the strategy of the interpolated start.

It is time to analyse more in detail the velocity distribution. Here are reported the **velocity magnitude** and the **Y-velocity** before and after the transition. The contours can help to understand the whole fluid-dynamic conformation.

The most important change generated by the evolution is the strong decrease in magnitude. All the final configurations present less intense velocity. It is interesting to see that the velocity magnitude is at the beginning more intense in the external part of the IV; with time it is slowly increasing both outside and towards the central part. So, a continuous evolution is going on.
As seen for the previous interpolation cases, the rotational spin is maintained. Furthermore, it is quite clear that in the bottom part of the vessel there is a soft difference. A

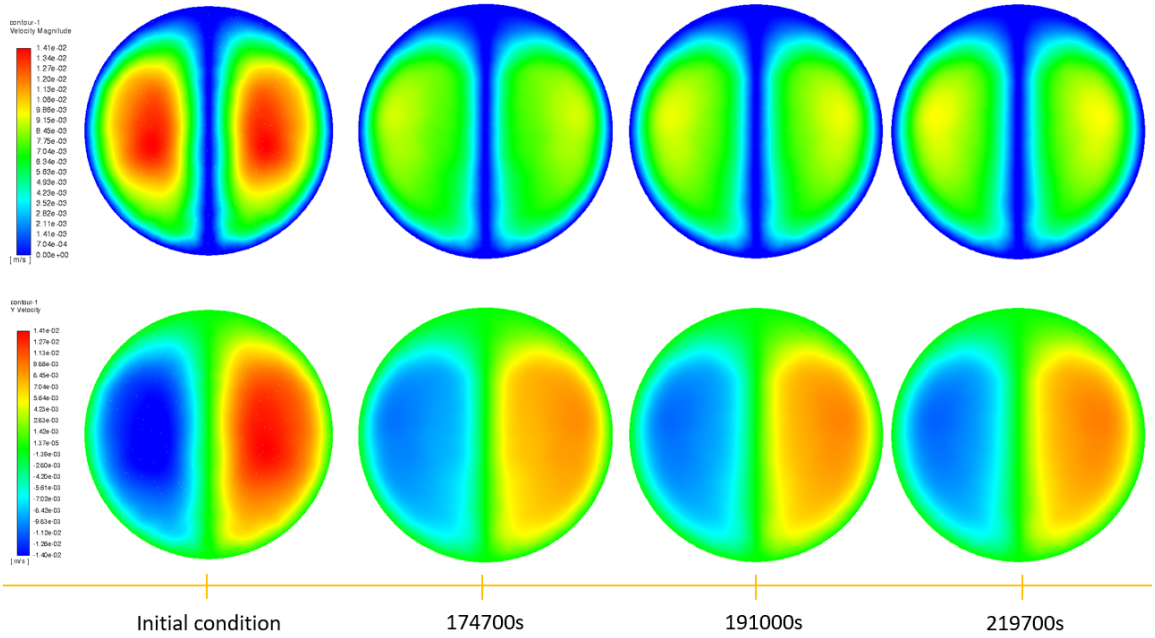

Figure 6.19. Velocity magnitude and Y-velocity evolution – ZX plane.

larger region is characterised by low velocities. Anyway, as just said, a slow adjustment is persistent. More accurate details are given in figure 6.20.

The plot below represents the velocity trend on the usual horizontal line of the ZX plane. It is given both the profile before and after the drop of the velocities.

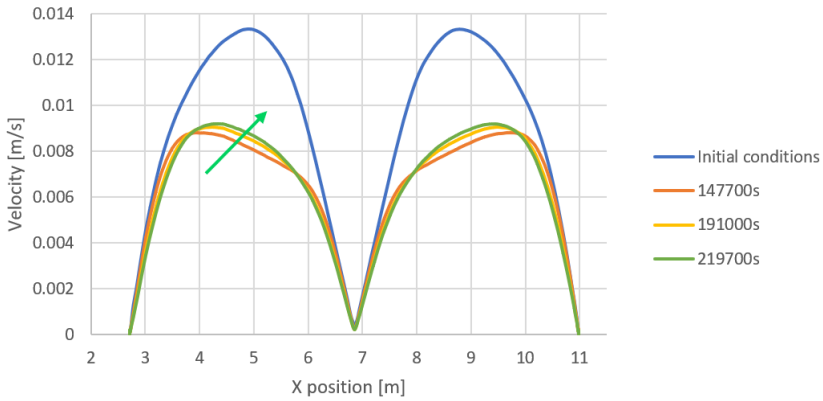

Figure 6.20. Velocity magnitude profile on a horizontal line – $Z = 5.85$m

It can be appreciated how the top of the profile is moving and rearranging towards a central and still symmetric distribution. Additionally, during this process the peak is very slowly moving up; this can explain the increasing trend of some monitored point in figure 6.18. After an initial lateral tendency, everything is returning to a more familiar distribution, supporting the considerations taken from the contours.

Finally, the comparison of the different velocity components and the boundary behaviour is presented. The table 6.4 contains the results of all the simulations

analysed until now. The maximum values of each category are reported.

N° cells	Surf.–Vol. [m^2 – m^3]	Average cell size [m]	Velocity at the boundary [m/s]	Vertical vel. [m/s]	Horizontal vel. [m/s]
270k	$5.67{\cdot}10^{1}$	0.0144684	$3.00{\cdot}10^{-4}$	$1.00{\cdot}10^{-6}$	$2.00{\cdot}10^{-5}$
530k	$5.67{\cdot}10^{1}$	0.0103432	$9.00{\cdot}10^{-4}$	$1.00{\cdot}10^{-6}$	$1.10{\cdot}10^{-5}$
2.4M	$3.22{\cdot}10^{2}$	0.0511671	$5.00{\cdot}10^{-4}$	$6.00{\cdot}10^{-5}$	$1.50{\cdot}10^{-4}$
5M	$3.22{\cdot}10^{2}$	0.0400625	$6.00{\cdot}10^{-4}$	$5.00{\cdot}10^{-5}$	$5.00{\cdot}10^{-4}$
10M	$3.22{\cdot}10^{2}$	0.0317976	$7.00{\cdot}10^{-4}$	$3.00{\cdot}10^{-5}$	$1.70{\cdot}10^{-4}$
10.2M	$3.22{\cdot}10^{2}$	0.0316047	$9.00{\cdot}10^{-4}$	$2.20{\cdot}10^{-5}$	$1.50{\cdot}10^{-4}$

Table 6.4. Geometry and fluid-dynamics results of the simulations.

The boundary velocity reaches the same magnitude of the bi-dimensional case. This is given by the equal layer structure and denotes a high resolution at least in the external region.
The vertical components is still decreasing, following the trend. The horizontal one, instead, returns at the value of the 2.4M cells grid.
Last, a mention should be done to the average cell size which, even if smaller, remains far from the 2D standards.

To summarise, the new structure for the boundary confirms its validity also in the 3D environment; the precision of the 2D results is achieved at the boundary. This solution is consequently implemented also in the last simulation.
The final 2.4M solution earns an added value, being a good starting point for the heavy cases and avoiding very time-consuming simulations.

6.4 Final simulation: extra fine mesh

The results coming from the heavier simulation are now presented. The extra fine with 20 millions of cells is the last employed computational grid. This represents the better tri-dimensional attempt we have to understand the fluid-dynamics of the system and to extrapolate a meaningful velocity field. The outputs of this model are then inserted in COMSOL Multiphysics in order to calculate a ^{210}Po concentration distribution.
Even if, as for the 10.2M cells, the simulation started from the interpolated values of the 2.4M case, the total length is remarkable. While the 10.2M case was run for two weeks, this final case took a period longer then a month to reach the same simulated time.

Doubling the number of computational cells, the target is to gain a more deep knowledge of the different velocity components. The same structure of layers of cells at the boundary is inserted in the mesh since, from the previous model, it was clear that it could bring to satisfying results. The BCs started from the beginning of the simulated period and the time-step is chosen to be $\Delta t = 4.5$s.

First of all, the monitored velocities in the usual spots, see fig. 6.2b, are shown.

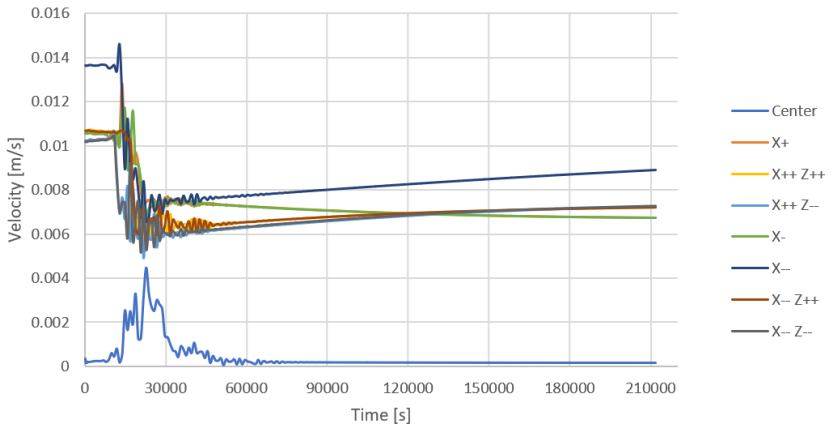

Figure 6.21. Velocity magnitude evolution.

The velocity trend is again evident from the plot. After few thousands of seconds a very strong decrease of the magnitudes is perceived. The blue line, describing the central point of the vessel, is telling us that the system felt the perturbation until 65'000s. Consequently, a new period of slow settlement is present.
The velocities are finally tending to a value around 0.007m/s, lower than the one reached in the 10.2M case. This of clearly coming from the better resolution of the system. This better mesh quality is probably the reason why the perturbation arrived sooner, check fig. 6.18.

The contours are a useful tool to immediately visualise the evolution. As before, the velocity magnitude and the Y-velocity are reported.

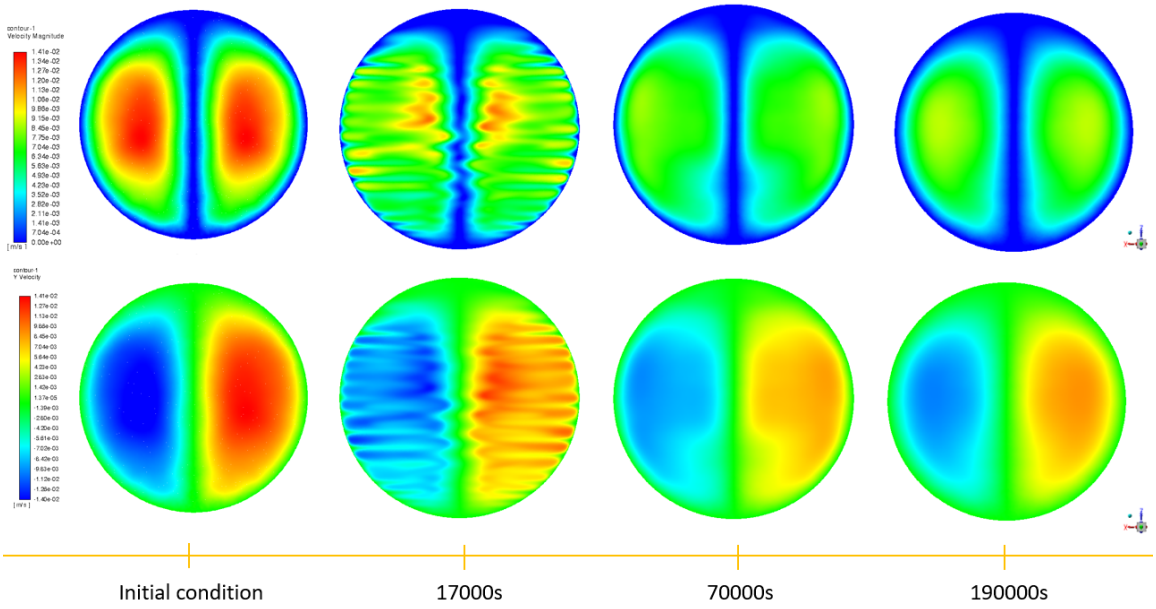

Figure 6.22. Velocity magnitude and Y-velocity evolution – ZX plane.

The general trend is not so different from the one of the 10.2M results. A view of the ZX plane during the transitory is also present, at 17'000s from the start. Thanks

to that particular picture, is visible how the effective rearrangement of the velocities is occurring. It happens following stratified structures at all the heights of the IV. Once this period is passed, the magnitudes stabilise to lower values.
The difference at the bottom is here more evident. There is a large region where the spin is soften and the velocity drops. With time, this part presents a slow increase of the magnitudes and the initial conformation is restored.
Once again, an area of higher movements, closer to the external part of the vessel, can be identified.

The velocity profile along the horizontal line at $Z = 5.85$m reveals the already seen phenomenon.

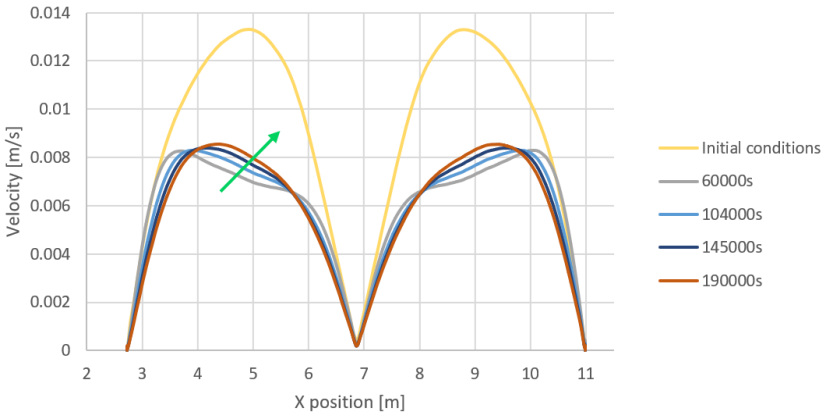

Figure 6.23. Velocity magnitude profile on a horizontal line – $Z = 5.85$m

After the general decrease of the magnitudes, the velocities started to slowly grow again towards the central part of the profile. The configuration is returning to have the peak around a position of $X = 4.65$m and the relatively symmetric point. The final profile will simply be a scaled version of the initial condition. The brown line, referred to 190'000s of simulation, is quite close to this ultimate situation.

The link between the velocity decrease and the increase of the number of cells is already been stressed. On the other hand, it could be wise to ask our-self how far we are from a final physical solution. A prevision of the needed n° of cells will be presented at the end of the present section.

The table below contains some relevant parameters of all the computed simulations, 2D and 3D. It is then possible to have a complete overview.

From the geometrical parameter of the average cell size it can be seen how the 20M cells grid has the lowest dimension. Anyway, this measure is still more than two times bigger than the bi-dimensional computational grid with 530k cells.
The behaviour at the boundary is equal to the 10.2M cells; the boundary structures reached the target.
The horizontal components finally turned to a downward trend. The values are still one order of magnitude too high compared to the 2D. The same conclusions can be taken for the vertical velocity.

N° cells	Surf.–Vol. [m^2 – m^3]	Average cell size [m]	Velocity at the boundary [m/s]	Vertical vel. [m/s]	Horizontal vel. [m/s]
270k	$5.67{\cdot}10^{1}$	0.0144684	$3.00{\cdot}10^{-4}$	$1.00{\cdot}10^{-6}$	$2.00{\cdot}10^{-5}$
530k	$5.67{\cdot}10^{1}$	0.0103432	$9.00{\cdot}10^{-4}$	$1.00{\cdot}10^{-6}$	$1.10{\cdot}10^{-5}$
2.4M	$3.22{\cdot}10^{2}$	0.0511671	$5.00{\cdot}10^{-4}$	$6.00{\cdot}10^{-5}$	$1.50{\cdot}10^{-4}$
5M	$3.22{\cdot}10^{2}$	0.0400625	$6.00{\cdot}10^{-4}$	$5.00{\cdot}10^{-5}$	$5.00{\cdot}10^{-4}$
10M	$3.22{\cdot}10^{2}$	0.0317976	$7.00{\cdot}10^{-4}$	$3.00{\cdot}10^{-5}$	$1.70{\cdot}10^{-4}$
10.2M	$3.22{\cdot}10^{2}$	0.0316047	$9.00{\cdot}10^{-4}$	$2.20{\cdot}10^{-5}$	$1.50{\cdot}10^{-4}$
20M	$3.22{\cdot}10^{2}$	0.0252508	$9.00{\cdot}10^{-4}$	$1.50{\cdot}10^{-5}$	$1.40{\cdot}10^{-4}$

Table 6.5. Geometry and fluid-dynamics results of the simulations.

The Z-component has the most unclear distribution, probably because generated by numerical noise. Thus, a more accurate look is given through the histograms representation in order to understand if the the solution is totally probabilistic or not. The bars represent the percentage of the points with the specified velocity on the x-axis.
The same graph for the 5M, 10.2M and 20M is reported in order to have a direct and easy comparison of the differences.

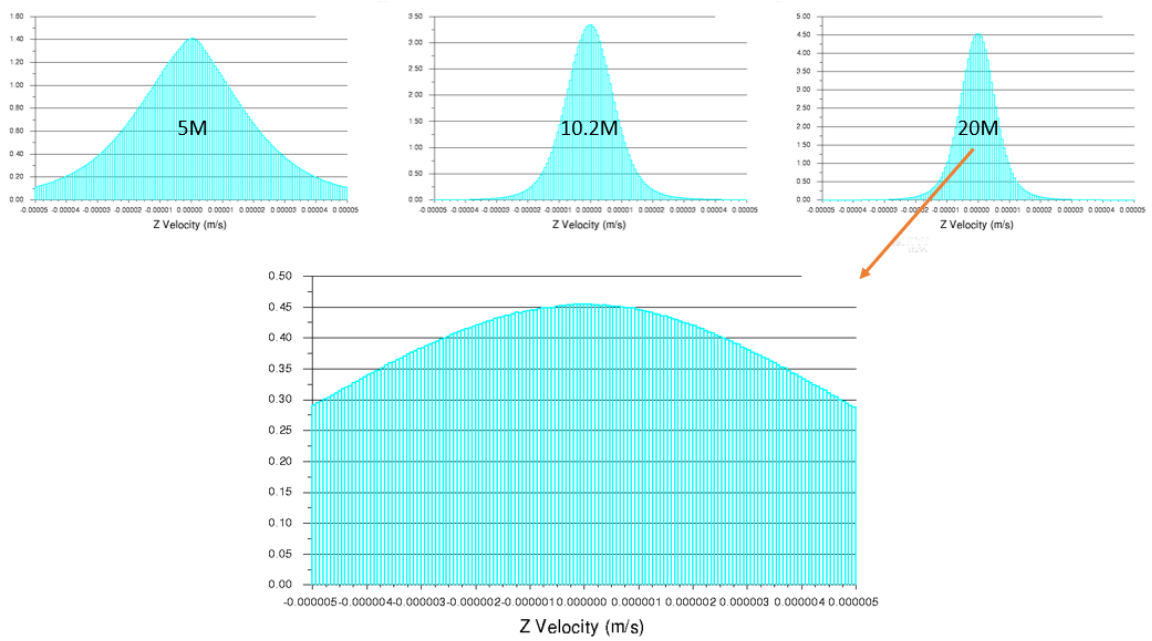

Figure 6.24. Z-velocity percentage distribution.

The first impression is to have a Gaussian distribution centred in zero. The variance is function of the number of cells; higher is the number, lower is the variance. This denotes a more precise and defined solution.
The behaviour seems to tell us the vertical component of the velocity has a probabilistic distribution approximated by a normal distribution. The detail of the 20M cells histogram is instead giving a different hint. From the plot data is possible to infer

that the distribution is centred in $0.8 \cdot 10^{-7}$m/s, and not in zero. Such a consideration could firstly appear useless, but, remembering the 2D trend visualised in figure 5.12, it is possible to find a link. The central value is small but very similar between the two cases. This is confirming that the 3D model is generally tending to the same solution of the bi-dimensional one and also the Z-velocities are following this path.

The path-lines, coloured by velocity magnitude, are reported in the next picture. The target is to understand if the particles are feeling the vertical components of the velocities or not. This way, it will be clear how much the field perceives the vertical movements. This lines are generated starting by the vertical ZX plane and following the velocity field with steps of 0.1m.

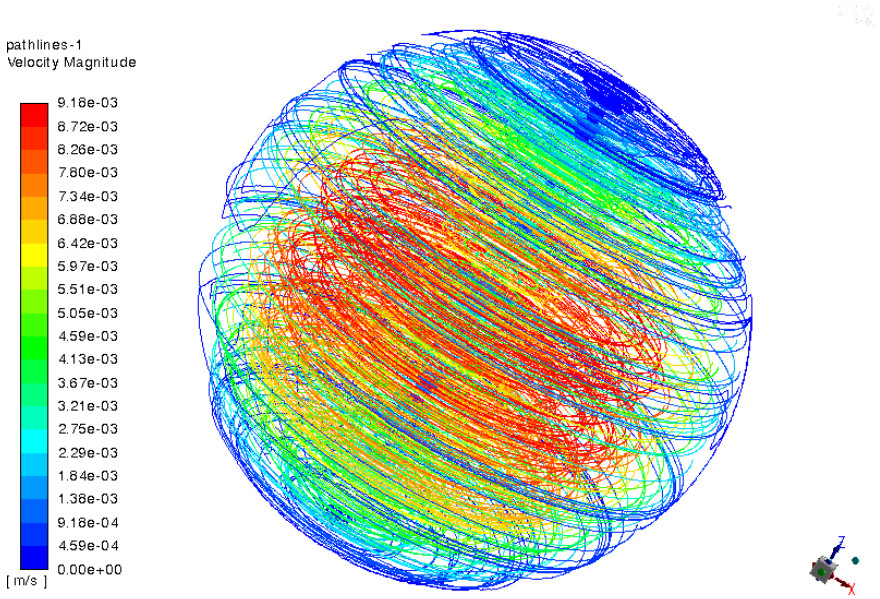

Figure 6.25. 3D path-lines coloured by velocity magnitude.

The path-lines are describing a very mature solution, the one which better approximates the 3D physical system. The fidelity of this image is quite high.
It appears that the vessel only perceives a pure rotation of the fluid around the vertical Z-axis. From an accurate study, no vertical inclination is seen inside the bulk. Only at the boundaries, some points reveal the tendency of a vertical motion; a similar behaviour has been previously described, but the initial more clear structures driven by the natural convection are now dumped. These vertical singularities, soon or later, are anyway starting to rotate with the same spin of the internal flow.

To summarise, the Z-velocity is slowly approaching the 2D distribution but it continuously maintains a Gaussian distribution which suggests a numerical noise nature. From the path-lines, no vertical directions are observed except on the boundary. Thus, the majority of vertical components are very small compared to the others and the whole velocity field is weakly influenced by them.

This analysis completes the pseudocumene fluid-dynamic study. Several comparisons of the solutions from different meshes are seen. A complete description of the

fluid behaviour in the IV is given.

6.4.1 Future studies for the fluid-dynamics

The Borexino detector IV fluid-dynamics has been characterised through the CFD modelling of the system. It is possible to say that the 2D results are quite satisfying, while the 3D models are still approaching the final physical configuration.
The aim of this brief paragraph is to give a concrete idea of how far we are from reaching a fully reliable description of the 3D system.

The following plots are describing the velocity evolution with the increase of the number of cells. The values are taken from the contours of the 3 simulations which reached a stable final solution, the coarse one, the very-fine and the extra-fine. The higher magnitudes are considered.

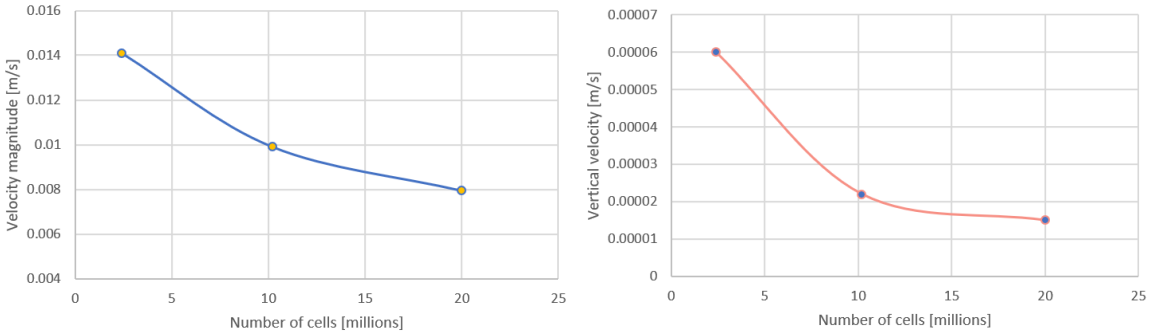

(a) (b)

Figure 6.26. Velocity trend as a function of the number of cells.

The message is quite clear. The velocities, here in particular the velocity magnitude and the Z-component, are falling in an asymptotic manner. This is confirming that the model is slowly approaching a final ad accurate solution.

Now, exploiting once again the value of the average cell size, a prediction of the number of cells needed to emulate the 2D computational grids can be made. This values are simply obtained turning the equation around.

N° of cells	Surf.–Vol. [m^2 – m^3]	Average cell size [m]
270k	$5.67 \cdot 10^1$	0.01446842
530k	$5.67 \cdot 10^1$	0.01034324
106M	$3.22 \cdot 10^2$	0.01446842
291M	$3.22 \cdot 10^2$	0.01034324

Table 6.6. Geometrical prevision for the possible future computational grids.

We can see how the total number of cells is very fast increasing. From a computational point of view, considering the Politecnico di Milano CFDLab, a mesh of 106M

of cells can be considered extremely heavy. A grid with 290M of cells cannot be used except through the employment of alternative computational resources.

For the future, a different approach could be exploited. A **pseudo-transient** simulation is under development. The idea is to initialise the model with a mature velocity field and maintain constant BCs. This way, going ahead in time exactly as a transient, the solution should faster converge. The final configuration is a 3D picture of the fluid distribution at a specific time. At the moment, the feedback is not good. It seems that the constant BCs are not able to generate a strong enough perturbation to reach the final results.

6.5 3D Polonium concentration

The final step of the tri-dimensional analysis is the polonium concentration calculation through the software COMSOL Multiphysics.
The ^{210}Po rate is always obtained in count per day every 100t of pseudocumene and the results are shown for the Fiducial Volume.

The values on horizontal lines in the ZX plane are visualised in order to check the radial distribution and the BCs.

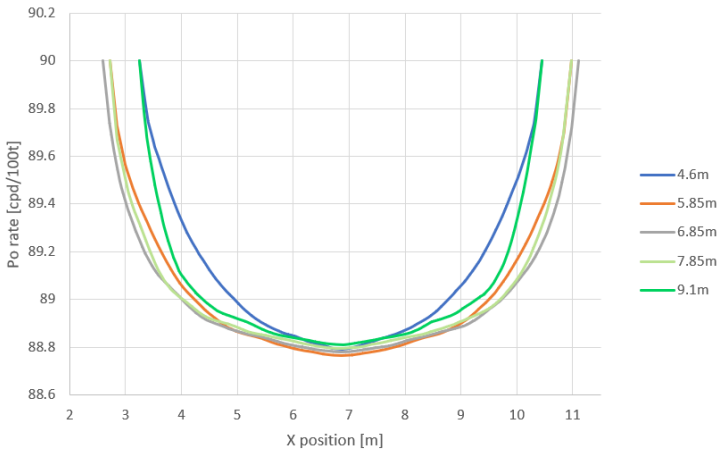

Figure 6.27. Polonium rate on horizontal lines – ZX plane

The trend reveals a familiar parabolic distribution since the polonium is migrating from the border of the IV towards the center. The rate is slightly lower in the higher part of the volume (green lines), this will be more clear from the next plots.

Here is reported a vertical distribution of the polonium concentration. The calculated values, for the 3D, are extracted from 21 horizontal XY planes at different heights of the FV. The mean value of every plane is computed and the trend is shown in the figure. The vertical coordinate now starts from zero at the bottom of the IV; this is how the measured values are taken. This way, the middle plane will coincide with a position of $Z = 4.25$m.

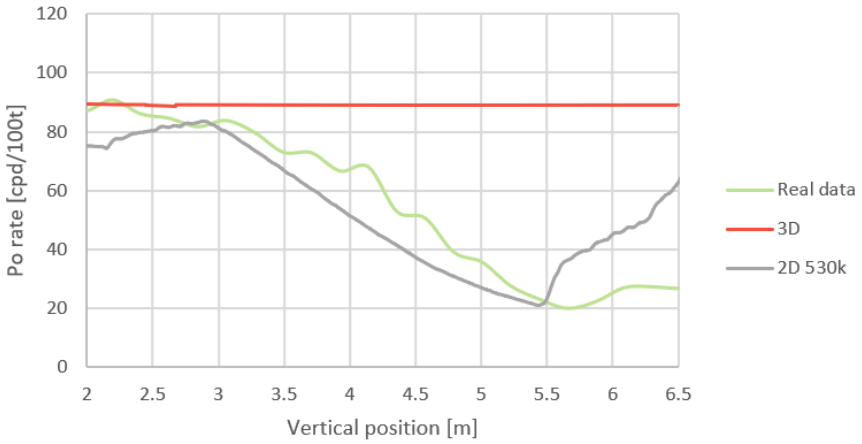

Figure 6.28. Vertical polonium distribution in the Fiducial Volume.

It is immediately evident that the 3D simulation gives a very higher rate. Whereas in the real case the concentration includes values between 90 and 20 cpd/100t, the calculated values are all around 89 cpd/100t. This is due to the velocity field which still presents velocities two order of magnitude stronger than the 2D case.
A focus only on the tri-dimensional outputs can give more information.

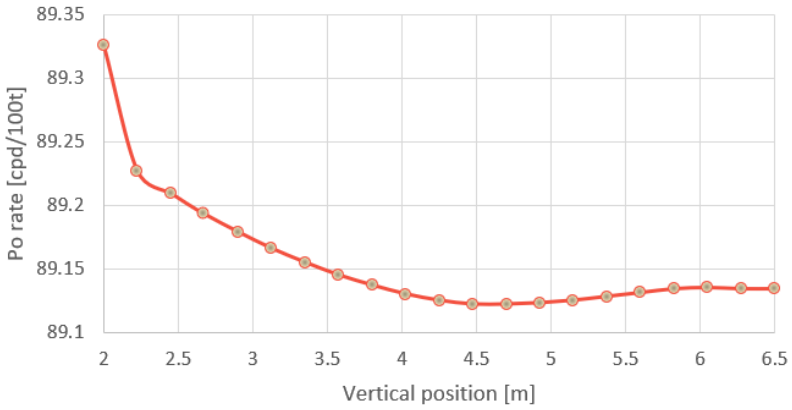

Figure 6.29. 3D calculated ^{210}Po rate.

A general similarity can be recognised. Indeed, lower concentrations are perceived in the topmost part of the FV. A minimum is found at 4.5m, for the measured rate it should be around 5.6m. The profile is at least similar.

In conclusion, the simulation is respecting the BCs and the general trend is suggesting that the model is only qualitatively reproducing reality. The distribution is quite comfortably; with a more precise velocity field the concentration will probably tend to the experimental data.

Conclusion and perspectives

The thesis revolves around the Borexino experiment. The problem regarding the neutrinos detector Inner Vessel background stability is approached. A considerable concentration of ^{210}Po reveals an energy spectrum within the neutrinos energy region. Thus, the internal fluid-dynamics of pseudocumene is investigated in order to reproduce the polonium movements.
Both bi-dimensional and tri-dimensional CFD models are designed. The fluid-dynamic model and the mass transfer model for the ^{210}Po are respectively built in *ANSYS* FLUENT and COMSOL Multiphysics. In the first case, the imposed boundary conditions are function of the temperature asymmetries of the air surrounding Borexino; this distribution brings to a clear internal isotherms stratification. Several computational grids are employed with the purpose of better understanding the inner movements, driven by natural convection.

The 2D simulations show that in the pseudocumene the flows are horizontally arranged. The velocity magnitude is in the order of $\mathcal{O}(10^5)$ m/s. The vertical velocities are instead one order of magnitude lower and their nature seems to be related to numerical noise. Beside the fluid-dynamic characterisation, a question about the precise position of a temperature sensor is considered. Two different linear interpolations are defined in order to precisely reproduce the system. The second brought to more satisfying results.
The ^{210}Po vertical concentration has been computed and compared between all the 2D cases. The model with a refined mesh of 530k cells is the one which better reproduces reality. The polonium rate is qualitatively and quantitatively acceptable, but the boundary temperature uncertainties, due to the unknown sensor position, cause a final inaccuracy.

The 3D model confirms the bi-dimensional behaviour and better characterises the overall fluid motion. This is what stands out in respect to the previous works: the best and very time consuming simulation describes the fluid movements as a pure rotation around the vertical axis of Borexino. As well, it is the explanation of the horizontal flows seen in the 2D cases. Some peculiarities are noted in the boundary areas, where few particles are directed in a vertical direction. All the velocity components are anyway one order of magnitude higher compared to their 2D equivalent. This is due to a too coarse mesh, even though the total number of cells and the computational efforts are remarkable.
Such a velocity field has an impact also on the polonium distribution. The vertical trend is indeed generally respected, but the concentration is extremely higher compared to reality.

It is clear that, given such small temperature asymmetries at the border, the fluid-

dynamics evolution of the pseudocumene is absolutely neither trivial nor foreseeable. Additionally, is underlined how little variations of the BCs could bring to considerable changes in the physics of the system. Thus, the presented 3D model, able to appreciate these features, gains a particular merit; several forward steps can of course be done in order to obtain more accurate results, adding value to the model itself.

For the next future a new kind of 3D simulation is under study. The pseudo-transient option could bring some benefits for both the needed time and the precision of the results. The general target is to find a way to use more refined meshes, always relying on the Polimi CFDLab. The second option is to exploit other computational resources which can easier handle heavier grids.

Acronyms

IV	Inner Vessel
CNO	Carbon–Nitrogen–Oxygen
CFD	Computational Fluid Dynamic
INFN	Istituto Nazionale di Fisica Nucleare
PMTs	Photomultipliers
CTF	Counting Test Facility
R&D	Research and Development
PC	Pseudocumene
FV	Fiducial Volume
DMP	Dimethylphthalate
SSS	Stainless Steel Sphere
BTMMS	Borexino Thermal Monitoring & Management System
LTPS	Latitudinal Temperature Probes System
WT	Water Tank
TIS	Thermal Insulation System
AGSS	Active Gradient Stabilisation System
BCs	Boundary Conditions
WR	Water Ring
BL	Boundary Layer
PISO	Pressure Implicit with Splitting of Operations
SIMPLE	Semi-Implicit Method for Pressure Linked Equations
MUSCL	Monotonic Upwind Scheme for Conservation Laws
CFL	Courant-Friedrichs-Lewy

Bibliography

[1] O. SmirnovG. BelliniJ. BenzigerD. BickG. BonfiniD. BravoB. CaccianigaF. CalapriceA. CaminataP. CavalcanteA. ChavarriaA. ChepurnovD. D'AngeloS. DaviniA. DerbinA. EmplA. EtenkoK. FomenkoD. FrancoG. FiorentiniC. GalbiatiS. GazzanaC. GhianoM. GiammarchiM. Göger-NeffA. GorettiC. HagnerE. HungerfordAldo IanniAndrea IanniV. KobychevD. KorablevG. KorgaD. KrynM. LaubensteinB. LehnertT. LewkeE. LitvinovichF. LombardiP. LombardiL. LudhovaG. LukyanchenkoI. MachulinS. ManeckiW. ManeschgF. MantovaniS. MarcocciQ. MeindlE. MeroniM. MeyerL. MiramontiM. MisiaszekP. MosteiroV. MuratovaL. OberauerM. ObolenskyF. OrticaK. OtisM. PallaviciniL. PappL. PerassoA. PocarG. RanucciA. RazetoA. ReB. RicciA. RomaniN. RossiR. SaldanhaC. SalvoS. SchönertH. SimgenM. SkorokhvatovA. SotnikovS. SukhotinY. SuvorovR. TartagliaG. TesteraD. VignaudR. B. VogelaarF. von FeilitzschH. WangJ. WinterM. WojcikA. WrightM. WurmO. ZaimidorogaS. ZavatarelliK. ZuberG. Zuzel. Solar neutrino with borexino: results and perspectives. *Phys. Part. Nuclei*, 46(2):166–173, 2015.

[2] Altenmüller K. Appel S. *et al.* Agostini, M. Comprehensive measurement of pp-chain solar neutrinos. *Nature*, 562:505–510, 2018.

[3] Gianpaolo Bellini, J Benziger, D Bick, G Bonfini, D Bravo, M Buizza Avanzini, B Caccianiga, L Cadonati, Frank Calaprice, P Cavalcante, et al. Final results of borexino phase-i on low-energy solar neutrino spectroscopy. *Physical Review D*, 89(11):112007, 2014.

[4] K. B. McCarty. *The Borexino nylon film and the third counting test facility.* PhD thesis, Princeton University, New Jersey, USA, 2006.

[5] G. Alimonti, C. Arpesella, H. Back, M. Balata, D. Bartolomei, A. de Bellefon, G. Bellini, J. Benziger, A. Bevilacqua, D. Bondi, S. Bonetti, A. Brigatti, B. Caccianiga, L. Cadonati, F. Calaprice, C. Carraro, G. Cecchet, R. Cereseto, A. Chavarria, M. Chen, A. Chepurnov, A. Cubaiu, W. Czech, D. D'Angelo, F. Dalnoki-Veress, A. De Bari, E. De Haas, A. Derbin, M. Deutsch, A. Di Credico, A. Di Ludovico, G. Di Pietro, R. Eisenstein, F. Elisei, A. Etenko, F. von Feilitzsch, R. Fernholz, K. Fomenko, R. Ford, D. Franco, B. Freudiger, N. Gaertner, C. Galbiati, F. Gatti, S. Gazzana, V. Gehman, M. Giammarchi, D. Giugni, M. Goeger-Neff, T. Goldbrunner, A. Golubchikov, A. Goretti, C. Grieb, C. Hagner, T. Hagner, W. Hampel, E. Harding, S. Hardy, F.X. Hartmann, R. von Hentig, T. Hertrich, G. Heusser, M. Hult, A. Ianni, An. Ianni, L. Ioannucci, K. Jaenner, M. Joyce, H. de Kerret, S. Kidner, J. Kiko, T. Kirsten, V. Kobychev, G. Korga,

G. Korschinek, Yu. Kozlov, D. Kryn, P. La Marche, V. Lagomarsino, M. Laubenstein, C. Lendvai, M. Leung, T. Lewke, E. Litvinovich, B. Loer, F. Loeser, P. Lombardi, L. Ludhova, I. Machulin, S. Malvezzi, A. Manco, J. Maneira, W. Maneschg, I. Manno, D. Manuzio, G. Manuzio, M. Marchelli, A. Martemianov, F. Masetti, U. Mazzucato, K. McCarty, D. McKinsey, Q. Meindl, E. Meroni, L. Miramonti, M. Misiaszek, D. Montanari, M.E. Monzani, V. Muratova, P. Musico, H. Neder, A. Nelson, L. Niedermeier, S. Nisi, L. Oberauer, M. Obolensky, M. Orsini, F. Ortica, M. Pallavicini, L. Papp, R. Parcells, S. Parmeggiano, M. Parodi, N. Pelliccia, L. Perasso, A. Pocar, R. Raghavan, G. Ranucci, W. Rau, A. Razeto, E. Resconi, P. Risso, A. Romani, D. Rountree, A. Sabelnikov, P. Saggese, R. Saldhana, C. Salvo, R. Scardaoni, D. Schimizzi, S. Schönert, K.H. Schubeck, T. Shutt, F. Siccardi, H. Simgen, M. Skorokhvatov, O. Smirnov, A. Sonnenschein, F. Soricelli, A. Sotnikov, S. Sukhotin, C. Sule, Y. Suvorov, V. Tarasenkov, R. Tartaglia, G. Testera, D. Vignaud, S. Vitale, R.B. Vogelaar, V. Vyrodov, B. Williams, M. Wojcik, R. Wordel, M. Wurm, O. Zaimidoroga, S. Zavatarelli, and G. Zuzel. The borexino detector at the laboratori nazionali del gran sasso. *Nuclear Instruments and Methods in Physics Research Section A: Accelerators, Spectrometers, Detectors and Associated Equipment*, 600(3):568 – 593, 2009.

[6] Michael Leung. *The Borexino Solar Neutrino Experiment: Scintillator purification and surface contamination.* PhD thesis, Princeton U., 2006.

[7] J. Benziger et al. The Nylon Scintillator Containment Vessels for the Borexino Solar Neutrino Experiment. *Nucl. Instrum. Meth.*, A582:509–534, 2007.

[8] W. M. Maneschg. *Low-energy solar neutrino spectroscopy with Borexino:Towards the detection of the solar pep and CNO neutrino flux.* PhD thesis, University of Heidelberg, Germany, 2011.

[9] A. P. Pocar. *Low background techniques and experimental challenges for Borexino and its nylon vessels.* PhD thesis, Princeton University, 2003.

[10] D. B. Berguño. *Precision Background Stability And Response Calibration in Borexino.* PhD thesis, Virginia Polytechnic Institute and State University, USA, 2016.

[11] D. Bravo-Berguño, R. Mereu, P. Cavalcante, M. Carlini, A. Ianni, A. Goretti, F. Gabriele, T. Wright, Z. Yokley, R.B. Vogelaar, F. Calaprice, and F. Inzoli. The borexino thermal monitoring & management system and simulations of the fluid-dynamics of the borexino detector under asymmetrical, changing boundary conditions. *Nuclear Instruments and Methods in Physics Research Section A: Accelerators, Spectrometers, Detectors and Associated Equipment*, 885:38 – 53, 2018.

[12] Thomas H Kuehn and Richard J Goldstein. An experimental study of natural convection heat transfer in concentric and eccentric horizontal cylindrical annuli. *Journal of Heat Transfer*, 100(4):635–640, 1 1978.

[13] V. K. Garg. Natural convection between concentric spheres. *International Journal of Heat and Mass Transfer*, 35:1935–1945, August 1992.

[14] 2015 ANSYS Inc. *Heat Transfer Modelling using ANSYS Fluent - Natural Convection*, December 2015.

[15] V. Di Marcello. *Borexino inner vessel fluid-dynamics, technical note*, March 2019.

[16] Particle In Cell Consulting LLC Westlake Village. *Interpolation using an arbitrary quadrilateral*, June 2012.

[17] H.K. Versteeg and W. Malalasekera. *An Introduction to Computational Fluid Dynamics*. PEARSON Education, Harlow, England, 2007.